Secondary inorganic aerosol chemistry and its impact on atmospheric visibility in over ammonia-rich urban area in central Taiwan

Li-Hao Young[a,*], Ta-Chih Hsiao[b], Stephen M. Griffith[e], Ya-Hsin Huang[a], Hao-Gang Hsieh[a], Tang-Huang Lin[c], Si-Chee Tsay[d], Yu-Jung Lin[a], Kuan-Lin Lai[a], Neng-Huei Lin[e], Wen-Yinn Lin[e]

[a]Department of Occupational Safety and Health, China Medical University, 100, Sec. 1, Jingmao Rd., Beitun Dist., Taichung 406040, Taiwan

[b]Graduate Institute of Environmental Engineering, National Taiwan University, 1, Sec. 4, Roosevelt Rd., Taipei 10617, Taiwan

[c]Center for Space and Remote Sensing Research, National Central University, 300, Zhongda Rd, Zhongli Dist., Taoyuan 320317, Taiwan

[d]NASA Goddard Space Flight Center, 8800, Greenbelt Road, Greenbelt, MD 20771, USA

[e]Department of Atmospheric Sciences, National Central University, 300, Zhongda Rd, Zhongli Dist., Taoyuan 320317, Taiwan

*Corresponding author. Tel.: +886-4-2205-3366 x.6219; Fax: +886-4-2299-2147; Email: lhy@mail.cmu.edu.tw (L.-H. Young)

24

25 **Graphical Abstract**

26

27
28
29
30 **Highlights**

31
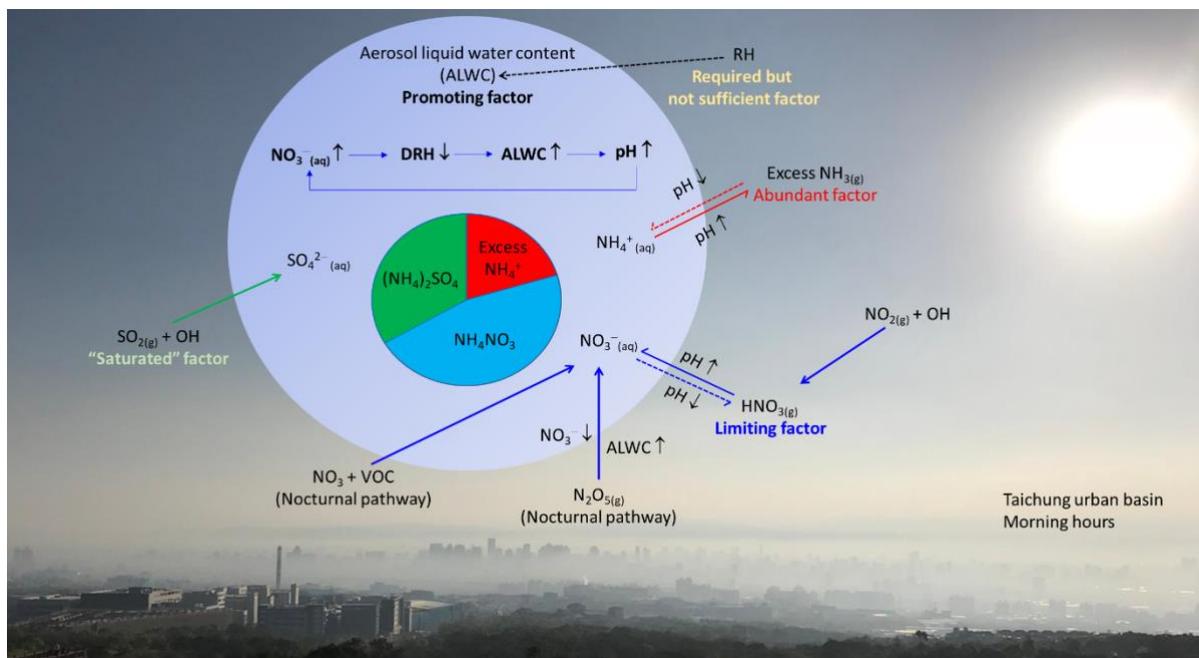
32 • Acidic/basic gases and $PM_{2.5}$ water-soluble ions were measured hourly in urban
33   air.
34 • Thermodynamic model was used to predict the inorganic aerosol system at
35   equilibrium.
36 • Only nitrate contribution to $PM_{2.5}$ increased with decreasing visibility.
37 • Mutual promotion of nitrate and aerosol water was key to impaired visibility.
38 • $PM_{2.5}$ was most sensitive to HNO_3 and hence NO_x, and relatively insensitive to
39   NH_3.

40
41

42

43 **Abstract**

44 This study investigated the hourly inorganic aerosol chemistry and its impact on

45 atmospheric visibility at an urban area in Taiwan, based on long-term measurements

46 of aerosol light extinction, inorganic gases (NH_3, HNO_3, HCl) and $PM_{2.5}$ water-

47 soluble ions (WSIs; SO_4^{2-}, NO_3^-, Cl^-, NH_4^+, Na^+, K^+, Ca^{2+} and Mg^{2+}) and the

48 ISORROPIA II thermodynamic equilibrium model. On average, the SO_4^{2-}, NO_3^- and

49 NH_4^+ (SNA) contributed to 90% of WSIs, which in turn made up about 50% of the

50 $PM_{2.5}$. The $PM_{2.5}$, SNA and aerosol pH, aerosol liquid water content (ALWC),

51 sulfur/nitrogen oxidation ratio all increased with decreasing visibility. In particular,

52 the NO_3^- contribution to $PM_{2.5}$ increased whereas the SO_4^{2-} contribution decreased

53 with decreasing visibility. The diurnal variations of the above parameters indicate that

54 the coupling of NO_3^- and ALWC were obvious under decreasing visibility, indicating

55 the mutual promotion between the two enhanced the aerosol hygroscopicity and

56 aqueous phase reactions conducive for NO_3^- formation. The ambient relative

57 humidity (RH) was a required but not sufficient condition for the elevated NO_3^-. The

58 thermodynamic model results show that the inorganic aerosol system in the study area

59 was characterized by excessive NH_3 and NH_4^+ under high RH (average 70.7%), under

60 which the $PM_{2.5}$ was most sensitive to HNO_3 and hence NOx, and relatively

61 insensitive to NH_3. Meantime, the SO_4^{2-} was fully neutralized and thus was not a

62 limiting but saturated factor for degrading visibility. Therefore, a reduction of NOx

63 would result in an instantaneous reduction of NO_3^-, $PM_{2.5}$, ALWC, and hence

64 improved visibility. On the other hand, a substantial amount of NH_3 reduction (73%)

65 is required such that $PM_{2.5}$ becomes sensitive to NH_3.

66

70

71

72

3

1. Introduction

Fine particulate matter ($PM_{2.5}$) is well known for its adverse impact on atmospheric visibility, as well as human health, and its role in Earth's radiative balance (Myhre et al., 2013; Pope et al., 2020; Pui et al., 2014). The extent of those impacts depends on the physicochemical properties of $PM_{2.5}$, such as the chemical composition, size distribution, hygroscopicity, mixing state and morphology. $PM_{2.5}$ speciation studies in cities around the globe show that its major composition includes inorganic water-soluble ions (WSIs) or salts, organic matter (OM), elemental carbon (EC), soil and sea salt (NaCl), among which the relative abundance varies across different locations (Cheng et al., 2016; Liang et al., 2016). However, the aerosol liquid water content (ALWC) associated with $PM_{2.5}$ is typically not being accounted by conventional sampling and analytical methods. In particular, sulfate (SO_4^{2-}), nitrate (NO_3^-) and ammonium (NH_4^+) (together referred to as SNA) are the major or dominant WSIs, which are primarily responsible for the uptake of ALWC. The most important gas-phase precursors of SNA are basic ammonia (NH_3) and acidic sulfur dioxide (SO_2) and nitrogen oxides ($NOx=NO+NO_2$). The latter two acidic gases could undergo gas-phase oxidation by hydroxyl radical (OH) during the daytime to form sulfuric acid (H_2SO_4) and nitric acid (HNO_3), respectively. With ozone (O_3), NOx could also be oxidized to gas-phase dinitrogen pentoxide (N_2O_5). In clouds or fogs, SO_2 oxidation is enhanced due to aqueous-phase reactions with hydrogen peroxide (H_2O_2), O_3 and oxygen (O_2). During the nighttime, the uptake of N_2O_5 by the ALWC on the aerosol surface could then lead to the formation of HNO_3. In a recent study, Yu et al. (2020) (Yu et al., 2020) showed that the measured N_2O_5 were typically below 0.2 ppb and the uptake coefficient averaged 0.026 in several cities in China. H_2SO_4 has very low vapor pressure and thus predominantly partitions to the aerosol phase. NH_3 reacts preferentially with H_2SO_4 over HNO_3 and forms ammonium sulfate (($NH_4)_2SO_4$) and/or bisulfate (NH_4HSO_4). After H_2SO_4 is completely neutralized, the excess NH_3 would then react with HNO_3 and HCl, forming ammonium nitrate (NH_4NO_3) and ammonium chloride (NH_4Cl). Because the SNA are mainly formed via atmospheric (photo)chemical reactions, they are also known as the secondary inorganic component of aerosols.

Atmospheric visibility is commonly perceived as an indicator of air quality, and is determined by the light scattering (b_s) and absorption (b_a) by ambient aerosols and gases, collectively known as light extinction (b_{ext}), with the aerosol contribution dominating over gases. The US Interagency Monitoring of Protected Visual Environments (IMPROVE) algorithm has been commonly used to estimate the contributions of individual $PM_{2.5}$ chemical components to b_{ext} under ambient RH (Malm et al., 1994; Pitchford et al., 2007; Watson, 2002). The $PM_{2.5}$ is assumed to

consist of $(NH_4)_2SO_4$, NH_4NO_3, soil, OM, EC and NaCl. The hygroscopicity of $(NH_4)_2SO_4$, NH_4NO_3 and NaCl is accounted by using the water growth term (f(RH)), which is mass-dependent for the former two salts. All $PM_{2.5}$ chemical components contribute to the aerosol light scattering (b_{sp}), as well as coarse particle ($PM_{2.5-10}$), except the EC that contributes to aerosol light absorption (b_{ap}). In addition, the gas scattering (b_{sg}) and absorption (b_{ag}) are attributed to Rayleigh scattering and NO_2, respectively. A number of earlier studies in Asia, particularly in China, have reported severely impaired visibility (i.e., haze events) and its relationship with $PM_{2.5}$ composition and meteorology (Cao et al., 2012; Fu et al., 2016; See et al., 2006; Shen et al., 2014; Szidat, 2009; Wang et al., 2012). The haze events were reported to be associated mainly with elevated SO_4^{2-}, OM and relative humidity (RH). In recent years, interestingly, numerous studies have shown that NO_3^- has become the main culprit of severe haze as well as $PM_{2.5}$ pollution (Fu et al., 2020; Hu et al., 2021; Tian et al., 2019; Wang et al., 2020; Wen et al., 2015; Zhang et al., 2021; Zhou et al., 2016). Such a change of focus may be related to a number of reasons as a result of a complex interplay among precursor gases and aerosol composition, and atmospheric conditions. For example, the substantial reduction of SO_2 emission and hence SO_4^{2-} could be offset by NO_3^- formation if both HNO_3 and sufficient NH_3 are available. The increase of NO_3^- formation has been observed even though NOx has been declining over the years (Fu et al., 2020), and such increase would lower the deliquescence RH and promotes enhanced ALWC uptake at moderate RH. Wang et al. (Wang et al., 2020) have shown that the increased ALWC in turn increases the aerosol pH and thus favors the partitioning shift from gas-phase HNO_3 to aerosol-phase NO_3^-. In addition, the ALWC could enhance the N_2O_5 uptake that leads to its hydrolysis to form NO_3^- (Yu et al., 2020) . Unlike nonvolatile SO_4^{2-}, NH_4NO_3 is semivolatile and in reversible equilibrium with gas-phase HNO_3 and NH_3, and thus could volatile under high temperature and low RH. Addressing the question about the chemical domains in which the $PM_{2.5}$ is sensitive to HNO_3 and/or NH_3 is becoming increasingly crucial for an effective control strategy to reduce $PM_{2.5}$ and improve visibility. Nenes et al. (Nenes et al., 2020) have shown that the transition between HNO_3-dominated and NH_3-dominated sensitivity rather consistently occurs at aerosol pH≈2 over variable levels of ALWC, suggesting the ALWC plays a more important role in determining the type of aerosol sensitivity. In specific, the transition aerosol pH varies with temperature and logarithmically with ALWC.

As shown above, the impaired visibility has been strongly linked to secondary inorganic aerosols. Thermodynamic models, e.g., ISORROPIA (Fountoukis and Nenes, 2007; Nenes et al., 1999) and AIM (Clegg et al., 1998; Wexler and Seinfeld, 1990), have been extensively used to obtain a more complete picture of the inorganic

149 aerosol system at equilibrium state. For example, ISORROPIA II solves the

150 thermodynamics of the $K^+–Ca^{2+}–Mg^{2+}–NH_4^+–Na^+–SO_4^{2-}–NO_3^-–Cl^-–H_2O$ aerosol

151 systems with data on gas plus particle phase (forward mode) or particle phase

152 (backward mode) assuming stable or metastable state. The model predicts the

153 concentration of species in gas, liquid and solid phase at equilibrium, and also

154 estimates the ALWC and aerosol pH. The aerosol pH (acidity) and its close

155 interactions with ALWC have great importance in the aqueous chemistry in the

156 atmosphere (Pye et al., 2020). During Beijing winter haze, Song et al. (Song et al.,

157 2018) showed that the forward mode is less sensitive to measurement errors, and NH_3

158 plays a more important role than ALWC in aerosol pH. Using ISORROPIA II, Guo et

159 al. (Guo et al., 2018) examined the sensitivity of aerosol NH_4NO_3 to NH_3 and NOx

160 controls in Europe, the United States and China of contrasting $PM_{2.5}$ levels and

161 meteorological conditions. They found that, regardless of location, $PM_{2.5}$ is sensitive

162 to NH_3 only when aerosol pH drops below a critical value of ~3. On the other hand,

163 Nenes et al. (Nenes et al., 2020) proposed a new conceptual framework that explicitly

164 considers ALWC, aerosol pH and temperature as the key factors in determining the

165 sensitivity of secondary inorganic WSIs. They showed that, regardless of location, the

166 transition between NH_3^--dominated and HNO_3-dominated sensitivity always occurred

167 at aerosol pH of ~2 but over a wide range of ALWC. As such, they suggested that the

168 limiting factor is the ALWC, whereas aerosol pH alone is not sufficient to determine

169 the type of sensitivity.

170   In Taiwan, a number of previous studies have attempted to link visibility with

171 aerosol composition and meteorology (Chen et al., 2014; Lee et al., 2012; Maurer et

172 al., 2019; Tsai, 2005; Tsai et al., 2007; Tsai and Cheng, 1999; Yuan et al., 2002). Most

173 of those studies relied on filter-based time-integrated samples for aerosol

174 composition, and thus could not resolve the highly dynamic aerosol chemistry

175 associated with impaired visibility. In a short intensive field study, on the other hand,

176 Chen et al. (2014) adopted hourly measurement techniques for aerosol composition

177 and illustrated the finer chemistry details that led to impaired visibility in Taichung,

178 Taiwan. Those earlier studies consistently showed that SO_4^{2-} played a major role,

179 along with stagnant air and high RH, in impairing visibility. More recently, a long-

180 term study by Ting et al. (Ting et al., 2021) used in-situ measurements of hourly $PM_{2.5}$

181 composition and identified the NO_3^- as the only chemical component with which its

182 fraction in $PM_{2.5}$ increased with decreasing visibility at a suburban site in Taichung.

183 The change of SO_4^{2-}-driven to NO_3^--driven impaired visibility requires further

184 examination. In addition, the inorganic aerosol chemistry (i.e., gas and aerosols) has

185 not yet been fully scrutinized. Here, we examine the hourly inorganic aerosol

186 chemistry at an NH_3-rich urban area in Taichung, Taiwan, using long-term hourly

187 measurements of HNO_3, NH_3 and $PM_{2.5}$ WSIs from 2017 to 2019. The monthly and

188 hourly variations of inorganic gases and aerosols were determined and related to

189 visibility (b_{ext}). The ISORROPIA thermodynamic equilibrium model was used to

190 explore gas-particle partitioning of NH_4NO_3, and the chemical regimes of WSIs

191 sensitivity to HNO_3 and NH_3 availability for policy implications.

192

193 **2. Methods**

194 **2.1 Study period and area**

195   The sampling campaign was conducted from September 2017 to September

196 2019, during which hourly measurements of HNO_3, NH_3 and $PM_{2.5}$ WSIs, aerosol

197 light extinction, gas pollutants and meteorological parameters were made

198 simultaneously. Fig. S1 shows the monitoring sites, industrial/science parks, and

199 major sources in the study area. The study area was in the basin area of urban

200 Taichung City (lower right corner in Fig. S1), which has a population density of

201 1273.6 people km^{-2} and is the 7th largest city located in the central part of Taiwan.

202 There are an industrial park and a science park nearby, to the northwest of the urban

203 area. Further away to the northwest and near the coastline, there are a coal-fired

204 power plant (5500 MW), a steel plant, a harbor and a few more industrial parks. The

205 monitoring of pollutants (except aerosol light extinction) was carried out in an air-

206 conditioned monitoring station, about 20 m adjacent to one of the Taiwan EPA air

207 quality monitoring sites, Zhongming (ZM) station (indicated as a star in Fig. S1),

208 nearby the urban center. Both stations are located on the rooftop of a school, where

209 the sample inlet was 17.5 m above ground level. About 6 km to the northwest of ZM

210 station is another satellite site (indicated as a circle in Fig. S1), where the aerosol light

211 extinction measurements were made inside an air-conditioned trailer with the

212 sampling height of 10 m above ground level.

213   The data on criteria air pollutants and meteorological parameters during the

214 study period were acquired from the Taiwan EPA-operated ZM station. The ZM

215 station is equipped with β-ray attenuation monitors for $PM_{2.5}$ and PM_{10} (Met One

216 BAM-1020; WINS impactor for $PM_{2.5}$), UV fluorescence spectrometer for SO_2

217 (Ecotech 9850B), IR analyzer for CO (Horiba APMA-360), chemilluminescence

218 detector for NOx (Ecotech 9841B) and nondispersive UV photometer for O_3 (Ecotech

219 9810B). In addition, it also houses a suite of metrological instruments for

220 measurements of ambient temperature/RH (Met One 083D), wind speed (Met One

221 014A), and wind direction (Met One 024A).

222

223 **2.2 Hourly inorganic gases and WSIs measurement**

224   A semi-continuous instrument, In-situ Gas and Aerosol Composition (IGAC)

225 monitoring system (Model S-611, Zhang Jia), was used to measure gas-phase NH_3,
226 HNO_3, HCl and $PM_{2.5}$ WSIs, including SO_4^{2-}, NO_3^-, Cl^-, NH_4^+, Na^+, K^+, Ca^{2+} and
227 Mg^{2+}. Details of the performance and application of IGAC are available in a number
228 of earlier studies (Feng et al., 2018; Liu et al., 2017, 2019; Ting et al., 2021; Wu et al.,
229 2019; Young et al., 2016). In brief, the IGAC draws ambient air at 16.7 L min^{-1}
230 through a series of PM_{10} impactor (Thermo Scientific) and a $PM_{2.5}$ cyclone. Acidic
231 and basic gases are absorbed by a Wet Annular Denuder (WAD) with dilute H_2O_2
232 solution based on gas diffusion. The $PM_{2.5}$ aerosols are collected by a SCrub and
233 Impact collector (SCI) that relies on the principles of wet scrubbing, particle growth
234 and impaction. The gas and aerosol liquid samples from the WAD and SCI are drawn
235 separately by a pair of syringe pumps that simultaneously collect (46 min) and then
236 alternatively inject the liquid samples to an in-line ion chromatography system
237 (Dionex ICS-3000) for the quantification of water-soluble anions and cations. The
238 method detection limits of the WSIs are in the range of 0.05 to 0.11 μg m^{-3} (Table
239 S1).
240   Quality assurance and control procedures were implemented on the measured
241 WSIs data. In specific, cation-to-anion (C/A, equivalent molar ratio) and anion-to-
242 cation (A/C) outliers were defined as those with values smaller than the small extreme
243 (SE = Q1 – 1.5IQR, where Q1 is the first quartile and IQR is the inter-quartile range)
244 value and those larger than the large extreme (LE = Q3 + 1.5IQR), and subsequently
245 removed from the dataset. The resulting data recovery rate was 85.3%, yielding
246 10,835 rows of hourly data. Fig. S2 presents the scatter plots of the molar equivalent
247 concentrations of cations versus anions, SO_4^{2-} versus NH_4^+, and (SO_4^{2-} + NO_3^-)
248 versus NH_4^+. The results show that, on average, their resulting regression slopes were
249 1.00, 1.48 and 1.03, respectively, indicating the neutrality of WSIs and the complete
250 neutralization of both SO_4^{2-} and NO_3^-. Yet, individual hourly data points were quite
251 variable about the 1:1 line. Finally, a pair-wise deletion was carried out such that
252 5,508 hours of data were available for thermodynamic modeling. The percentage of
253 data for each season is as follow: 27% in spring (Mar-May), 12% in summer (Jun-
254 Aug), 17% in fall (Sep-Nov) and 43% in winter (Dec-Feb).
255   The extent of neutralization of the two major ions NO_3^- and SO_4^{2-} by NH_4^+, and
256 all acidic gases and water-soluble inorganic anions by total NH_3 (TNH_3) was
257 evaluated by means of charge balance, with which the excess (or deficiency) of NH_4^+
258 and TNH_3 could be determined, as follow.
259

260 $$\text{Required } NH_4^+ = 18 \times \left(\frac{[SO_4^{2-}]}{48} + \frac{[NO_3^-]}{62} \right) \tag{1}$$

261 $$\text{Excess } NH_4^+ = \text{Measured } NH_4^+ - \text{Required } NH_4^+ \tag{2}$$

262 $$\text{Required } NH_3 = 17 \times \left(\begin{matrix} \frac{[SO_4^{2-}]}{48} + \frac{[NO_3^-]}{62} + \frac{[Cl^-]}{35.5} + \frac{[HNO_3]}{63} + \\ \frac{[HCl]}{36.5} - \frac{[Na^+]}{23} - \frac{[K^+]}{39} - \frac{[Ca^{2+}]}{20} - \frac{[Mg^{2+}]}{12} \end{matrix} \right) \qquad (3)$$

263 $$\text{Total } NH_3 = 17 \times \left(\frac{[NH_4^+]}{18} + \frac{[NH_3]}{17} \right) \qquad (4)$$

264 $$\text{Excess } NH_3 = \text{Total } NH_3 - \text{Required } NH_3 \qquad (5)$$

265

266

267 2.3 Aerosol light extinction measurement

268   A seven-wavelength aethalometer (AE33, Magee Scientific) was used to measure
269 the b_{ap} of $PM_{2.5}$ at the wavelengths of 370, 470, 520, 590, 660, 880 and 950 nm with
270 time-resolution of 1 min and a flow rate of 5 L min^{-1}. The b_{sp} of $PM_{2.5}$ was measured
271 with an integrating nephelometer (Model 3563, TSI) at three wavelengths of 450, 550
272 and 700 nm, and only the b_{sp} at 550 nm was used because human vision is most
273 sensitive to the wavelength of 550 nm (i.e., the green region of the visible light
274 spectrum). As such, the b_{ap} at 550 nm was interpolated using the absorption Ångström
275 exponent (AAE) at 370 nm and 880 nm as follow.

276

277 $$\text{AAE} = -\frac{\ln[b_{ap}(370)/b_{ap}(880)]}{\ln(370/880)} \qquad (6)$$

278 $$b_{ap}(550) = b_{ap}(880) \left(\frac{550}{880} \right)^{-AAE} \qquad (7)$$

279

280   In this study, the b_{ext} (Mm^{-1}) is the sum of b_{ap} and b_{sp}, ignoring the light
281 scattering and absorption by gases (b_{sg} and b_{ag}). It is important to note that the above
282 b_{ext} is more representative of the dry condition due to the heating effect from the
283 halogen lamp of the nephelometer (Fierz-Schmidhauser et al., 2010). In addition, the
284 b_{ext} under ambient RH greater than 90% were excluded in the present discussion to
285 separate potential fog events from haze events (Cai et al., 2018; Luan et al., 2018).

286

287 2.4 Inorganic aerosol equilibrium modeling

288   The ISORROPIA II thermodynamic equilibrium model was used to determine
289 the composition, phase state and gas-particle partitioning of the inorganic aerosol
290 system (Fountoukis and Nenes, 2007; Song et al., 2018; Yu et al., 2005; Zhang et al.,
291 2002). The model was run with the forward mode with the inputs of measured
292 ambient temperature, RH, gas-phase HNO_3, NH_3, HCl, and $PM_{2.5}$-phase SO_4^{2-}, NO_3^-,
293 Cl^-, NH_4^+, Na^+, K^+, Ca^{2+} and Mg^{2+}, assuming metastable equilibrium state (i.e., no
294 precipitation of salts). The forward mode has been shown to be more accurate and

295　robust (Song et al., 2018), whereas the metastable equilibrium state is more suitable

296　for the study area with the average RH > 70% (Guo et al., 2018). The timescale for

297　sub-micrometer (< 1 μm) and coarse (1 – 2.5 μm) particles to reach equilibrium had

298　been estimated to be less than 0.5 hr and more than 1 hr, respectively (Fountoukis et

299　al., 2009; Meng and Seinfeld, 1996). ==Table S2== shows the predicted gas and WSIs

300　concentrations were in good agreement with the observed concentrations, except for

301　gas-phase HNO_3 and HCl because of their low concentrations (< 0.5 ppb; see Section

302　3.2) and potential sampling losses under high RH environment. The predicted aerosol

303　pH and ALWC were used in the PM sensitivity analysis, given in the following

304　section.

305

306　**2.5 PM sensitivity analysis**

307　　Aerosol-phase, semivolatile NH_4NO_3 has become more and more prominent in

308　elevated $PM_{2.5}$ and severely impaired visibility in many Asian cities. Here, the $PM_{2.5}$

309　sensitivity to changes in HNO_3 and NH_3 was evaluated in relation to aerosol pH and

310　ALWC according to the new conceptual framework proposed by Nenes et al. (Nenes

311　et al., 2020). The fraction of NO_3^- and NH_4^+ partitioning in the aerosol phase at

312　equilibrium are denoted as $\varepsilon(NO_3^-)$ and $\varepsilon(NH_4^+)$, respectively, and can be calculated

313　according to the dissolution and dissociation reactions of HNO_3 and NH_3 (Guo et al.,

314　2017; Nenes et al., 2020; Song et al., 2018), as follow.

315

316
$$\varepsilon(NO_3^-) = \frac{K_{n1}H_{HNO_3}W_iRT}{\gamma_{H^+}\gamma_{NO_3^-}[H^+]+K_{n1}H_{HNO_3}W_iRT} \tag{8}$$

317

318
$$\varepsilon(NH_4^+) = \frac{\left(\gamma_{H^+}[H^+]/\gamma_{NH_4^+}\right)H_{NH_3}W_iRT}{1+\left(\gamma_{H^+}[H^+]/\gamma_{NH_4^+}\right)H_{NH_3}W_iRT} \tag{9}$$

319

320　where K_{n1} is the dissociation constant, H is the Henry's constant, W_i is the ALWC

321　associated with inorganic WSIs, R is the gas constant, γ is the activity coefficient, T is

322　the temperature and $[H^+]$ is the hydrogen ion concentration. For a given W_i, Eqs. (8)

323　and (9) yield two sigmoidal functions (also known as the S-curve) that give a

324　characteristic pH-sensitive range, between which a small change of aerosol pH results

325　in a large change of $\varepsilon(NO_3^-)$ and $\varepsilon(NH_4^+)$. An increase of aerosol pH would increase

326　$\varepsilon(NO_3^-)$ but decrease $\varepsilon(NH_4^+)$, whereas a decrease of aerosol pH has an opposite

327　effect. An arbitrary threshold of $\varepsilon(NO_3^-) = \varepsilon(NH_4^+) = 0.1$ was used to identify the

328　characteristic aerosol pH beyond or below which a substantial increase of $\varepsilon(NO_3^-)$ or

329　$\varepsilon(NH_4^+)$ is anticipated.

330

3. Results and Discussion

3.1 Meteorology, air quality and visibility

The meteorological conditions and air quality during the study period are given in Table S3. The hourly averages of ambient temperature, RH and wind speed (WS) were 22.4 °C, 70.7% and 1.4 m s^{-1}, respectively. The prevailing wind direction was north and northeasterly winds (Fig. S3). It is notable that the low WS and hence stagnant condition (<0.5 m s^{-1}) is very common in the urban area, due to its basin geology and surrounding elevated terrain that impede air flow movements (Fig. S1). The hourly averages of PM$_{2.5}$, SO$_2$, CO, O$_3$, NO and NO$_2$ were 22.9 μg m^{-3}, 2.3 ppb, 0.46 ppm, 28.0 ppb, 4.8 ppb and 18.3 ppb, respectively. Table 1 shows that the hourly averages of b$_{ap}$, b$_{sp}$ and b$_{ext}$ were 76.5, 28.3 and 103.2 Mm^{-1}, respectively. On average, the b$_{sp}$ dominated and contributed to 74% of the b$_{ext}$. Our earlier work showed that the IMPROVE-derived "wet" b$_{ext}$ is a factor of 2 to 6 higher than the Aethalometer-derived "dry" b$_{ext}$ at the satellite site of this study (Ting et al., 2021). In a 24-city study in China, Cheng et al. (Cheng et al., 2017) showed that dry PM$_{2.5}$ extinction (40.3%) and its hygroscopic extinction (54.6%) dominated the total b$_{ext}$ (b$_{sp}$ + b$_{ap}$ + b$_{sg}$ + b$_{ag}$). Their observed dry PM$_{2.5}$ extinction averaged 305.8 Mm^{-1}, which is considerably higher than that in this study. This is not surprising as the observed PM$_{2.5}$ ranged from 38.1 to 127.2 μg m^{-3}, which is a factor of 1.7 to 5.6 higher than the present study. The percentile values of b$_{ext}$ in Table 1 were used to divide the data into four visibility classes (i.e., quartiles, Q1, Q2, Q3 and Q4) for discussion in relation to changes in visibility. As shown, the contribution of b$_{sp}$ to b$_{ext}$ clearly increased with decreasing visibility, suggesting aerosol light scattering is the key factor affecting visibility and becomes even more dominant under severely impaired visibility.

Table 1. Summary statistics of measured aerosol light scattering, absorption and extinction (Mm^{-1}).

	b$_{sp}$	b$_{ap}$	b$_{ext}$
N	4001	4255	3735
Mean	76.5	28.3	103.2
SD	61.6	18.5	74.8
RSD	0.80	0.65	0.73
25th percentile	34.1	15.4	51.3
50th percentile	59.1	24.2	83.7
75th percentile	100.1	36.4	135.2

N is the sample size (hourly data), SD is the standard deviation, and RSD is the relative standard deviation.

356

3.2 Diurnal PM$_{2.5}$, aerosol light scattering and major water-soluble ions

The measured basic and acid gases, and PM$_{2.5}$ WSIs during the study period are given in Table 2. The average NH$_3$, HNO$_3$ and HCl were 11.9, 0.21 and 0.32 ppb, whereas the average major ions SO$_4^{2-}$, NO$_3^-$ and NH$_4^+$ (SNA) were 5.66, 5.10 and 3.71 μg m^{-3}, respectively. On average, the SNA contributed to 90% of the total WSIs, which in turn made up about 50% of PM$_{2.5}$. The average concentrations of the remaining minor ions were all less than 1 μg m^{-3}. Fig. S4 shows the monthly averages of the SNA. As expected, all three major ions were positively correlated with each other on a monthly basis. The major ions had minimum concentrations during the summer, and higher concentrations during the winter and spring, similar to that reported in Hong Kong (Griffith et al., 2015). Such seasonal differences are likely attributable to the stronger atmospheric instability (i.e., vertical mixing and elevated mixing height) in the summer than other seasons. The diurnal variations of PM$_{2.5}$, b$_{ext}$, b$_{sp}$, b$_{ap}$, SO$_4^{2-}$, NO$_3^-$ and NH$_4^+$ are given in Fig. 1. As shown, the PM$_{2.5}$ and b$_{ext}$ were correlated and were relatively higher during the nighttime than the daytime, but each had a daytime peak at different time of day. The b$_{ext}$ peaked at 0700 local time (LT) due to the increased b$_{ap}$, which was likely associated with the soot or black carbon emitted by morning rush-hour traffic. The PM$_{2.5}$ peaked a few hours later at 1000 LT, suggesting its secondary nature. It is notable that the b$_{sp}$ were also higher in the nighttime, and gradually decreased in the daytime to a minimum at 1500 LT. These results show that the visibility was generally better in the daytime.

378

379

380

Table 2. The measured basic and acidic gases, and PM$_{2.5}$ WSIs during the study period.

	NH$_3$	HNO$_3$	HCl	Na$^+$	NH$_4^+$	K$^+$	Ca^{2+}	Cl$^-$	NO$_3^-$	SO$_4^{2-}$
N	5458	4987	4733	5508	5508	5508	5508	5508	5508	5508
Mean	11.9	0.21	0.32	0.29	3.71	0.55	0.07	0.69	5.10	5.66
SD	5.8	0.17	0.28	0.17	3.48	0.86	0.05	0.65	5.83	3.56
RSD	0.49	0.82	0.86	0.59	0.94	1.57	0.76	0.95	1.14	0.63

Gaseous species are in ppb, and particulate species in μg m^{-3}.

The measured Mg^{2+} were below the MDL of 0.12 μg m^{-3}.

381

382
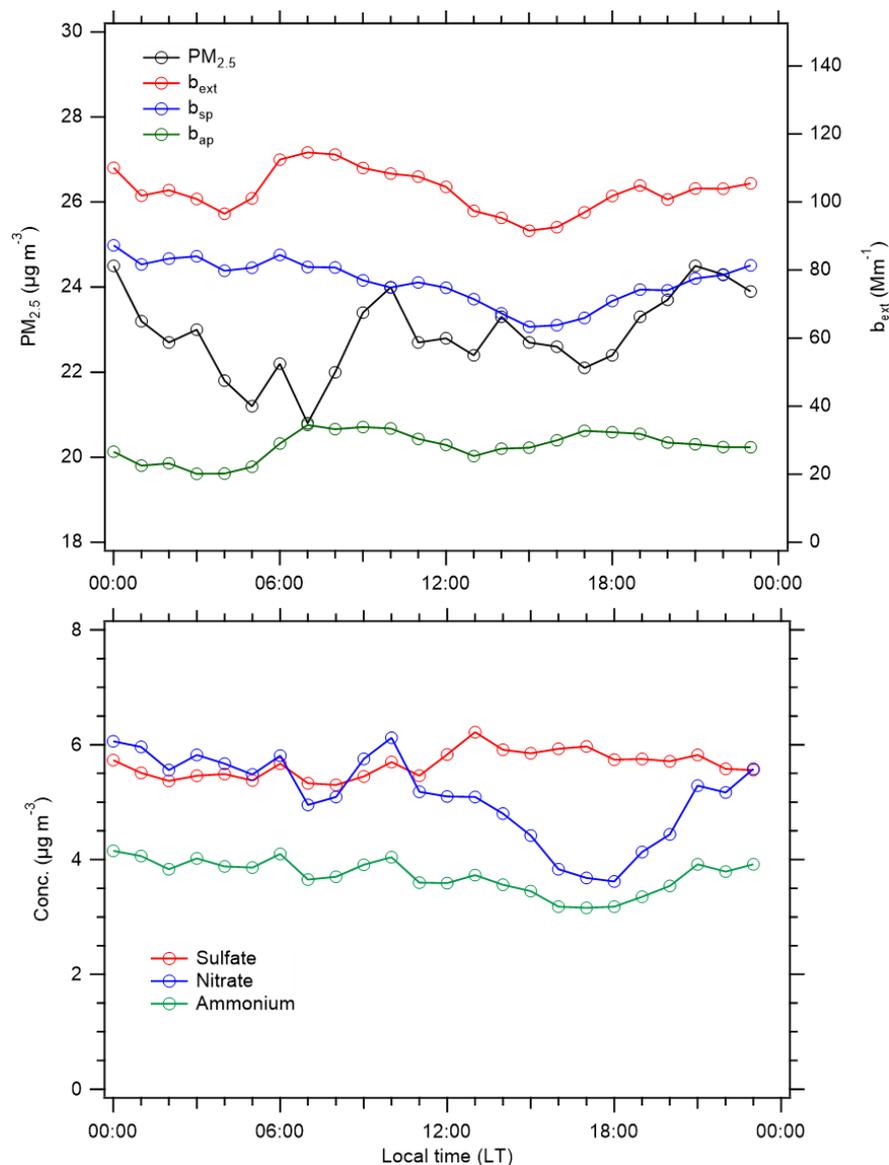
Fig. 1. The diurnal variation of hourly $PM_{2.5}$, b_{ext}, b_{sp}, b_{ap}, SO_4^{2-}, NO_3^- and NH_4^+.

The NO_3^- had a peak at 1100 LT, closely followed by NH_4^+, and both began to decrease in the afternoon to a minimum at about 1800 LT, and then increased rather sharply into late night. The conversion of NOx to NO_3^- is known to include four pathways: 1) the oxidation of NO_2 by OH in daytime, 2) the hydrolysis of N_2O_5 on aerosol surface at night, 3) the reduction of nitrate radical (NO_3) by hydrocarbons at night, and 4) the condensation of HNO_3 on aerosol surface (Seinfeld and Pandis, 2016; Zhang et al., 2021). Because the NO_3^- peak at 1100 LT occurred a few hours after the morning rush hours (NOx peak), it was likely that the two gas-phase pathways (1) and (4) were driving the elevated NO_3^- in the daytime. The simultaneous increases of NO_3^- and NH_4^+ in the evening hours suggest that the two aqueous-phase (nocturnal) pathways (2) and (3) were likely in play. For example, the

397 reduction of NO_3^- in the early evening and increasing RH in the evening favor the

398 uptake and subsequent hydrolysis of N_2O_5 (Yu et al., 2020). These two aqueous-phase

399 processes may also be responsible for the moderate, stable levels of NO_3^- and NH_4^+ in

400 the early morning, between 0000 to 0600 LT. Non-parametric wind regression (NWR)

401 plots revealed that elevated NO_3^- and NO_2 were considerably more localized, whereas

402 elevated NH_4^+ and NH_3 were slightly less localized and may have a strong source

403 region to the southwest of the study area (Fig. S5).

404　　　Unlike NO_3^- and NH_4^+, the SO_4^{2-} had a more obvious peak after noontime at

405 1300 LT, when the photochemistry was expected to be the strongest, suggesting the

406 SO_2 oxidation by OH was the primary formation mechanism of SO_4^{2-}. In addition, the

407 SO_4^{2-} appeared to be decoupled from NO_3^- and NH_4^+, and maintained at a relatively

408 stable concentration throughout the afternoon and evening. These results indicate that

409 the SO_4^{2-} formation was favored in the afternoon when the OH was limited and thus

410 suppressed the NO_3^- formation via the gas-phase, photochemically-driven pathways

411 (1) and (4). The higher ambient temperature, lower RH and stronger atmospheric

412 mixing in the afternoon may also contributed to the NO_3^- suppression due to

413 evaporation, lower aerosol pH and dilution, respectively. The simultaneous reductions

414 of NO_3^- and NH_4^+ clearly shows that NO_3^- was the limiting factor of the enhanced

415 NH_4^+ formation, independent of SO_4^{2-}. Unlike NO_3^- and NH_4^+, the NWR plots show

416 that elevated SO_4^{2-} and SO_2 were not only more spatially widespread but also had a

417 strong source to the northwest-west of the study area where there are a number of

418 major point sources (Fig. S5).

419

420 **3.3 Inorganic aerosol characteristics under impaired visibility**

421　　　In this section, we discuss the inorganic aerosol characteristics during impaired

422 visibility by dividing the dataset into four visibility classes (i.e., quartiles) according

423 to the percentile values of b_{ext} shown in Table 1. In specific, the first quartile (Q1) had

424 the best visibility, whereas the fourth quartile (Q4) had the poorest visibility. Fig. 2

425 presents the $PM_{2.5}$, SNA (SO_4^{2-} + NO_3^- + NH_4^+), ALWC and RH under different

426 visibility classes. The results clearly show that the $PM_{2.5}$, SNA and ALWC were

427 coupled and thus all increased substantially with decreasing visibility, consistent with

428 earlier studies (Hu et al., 2021; Shen et al., 2014; Zhou et al., 2016). The increases

429 were in the range of 3.7 to 4.6-fold. The ambient "wet" $PM_{2.5}$ (= $PM_{2.5}$ + ALWC) was

430 on average a factor of 1.79 higher than BAM-measured "dry" $PM_{2.5}$ (Fig. S6) due to

431 the heating of aerosol sampling inlet. Therefore, it is clear that measured "dry" $PM_{2.5}$

432 alone could not fully explain the visibility (Cheng et al., 2017; Yi et al., 2020), albeit

433 the two are moderately correlated. The average RH, however, was relatively

434 invariable across different visibility classes. On the outset, this appears that the RH

435 did not play much of a role in the changes of PM$_{2.5}$ inorganic composition, ALWC

436 and visibility. However, a more refined analysis suggests otherwise, which will be

437 discussed in later sections.

438
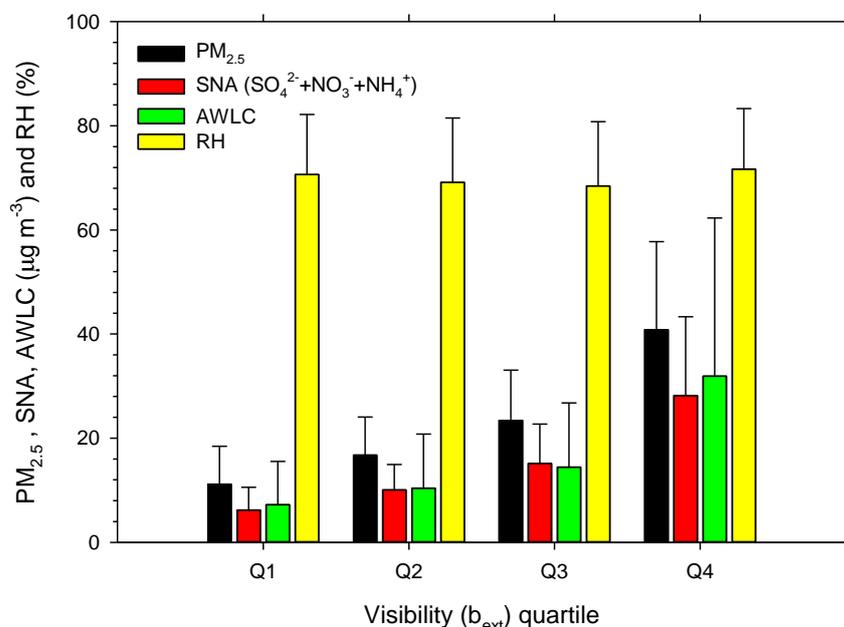
439

440 Fig. 2 The PM$_{2.5}$, SNA (SO$_4^{2-}$ + NO$_3^-$ + NH$_4^+$), ALWC and RH under different

441 visibility classes, Q1 (1st quartile; best visibility), Q2, Q3 and Q4 (poorest visibility).

442

443 Fig. 3 shows the WSIs concentrations and their respective contributions under

444 different visibility classes. As shown, all WSIs increased with decreasing visibility,

445 but their individual contributions to the total WSIs varied over different visibility

446 classes. In particular, the NO$_3^-$ contribution increased from 18.8% to 38.2%, whereas

447 the SO$_4^{2-}$ contribution decreased from 51.5% to 33.6% with decreasing visibility. The

448 NH$_4^+$ contributions increased slightly from 17.9% to 21.3%. These results strongly

449 suggest that NO$_3^-$ was the dominant WSI under severely impaired visibility, whereas

450 SO$_4^{2-}$ was the dominant WSI under good visibility. Such an increasing role of NO$_3^-$ in

451 severely impaired visibility has been reported in a number of studies (Fu et al., 2020;

452 Hu et al., 2021; Tian et al., 2019; Wang et al., 2020; Wen et al., 2015; Zhang et al.,

453 2021; Zhou et al., 2016). The inverse relationships between the relative contributions

454 of NO$_3^-$ and SO$_4^{2-}$ to PM$_{2.5}$ (expressed as fraction), along with ALWC and RH

455 changes, are more clearly illustrated between Q1 and Q4 of contrasting visibility (Fig.

456 4). As shown, regardless of visibility conditions, the NO$_3^-$ fraction increased whereas

457 the SO$_4^{2-}$ fraction decreased with increasing ALWC, which was positively correlated

458 with RH. It is important to note that the NO$_3^-$ and SO$_4^{2-}$ fractions were rather

459 invariant with RH changes. This highlights that the RH is a required but not sufficient

460 condition for increases of NO_3^-, whereas the ALWC appears to be more directly

461 related to the increases of NO_3^-. Wang et al. (Wang et al., 2020) recently showed the

462 mutual promotion between ALWC and NO_3^- that can rapidly enhance PM mass and

463 degrade visibility within a day.

464
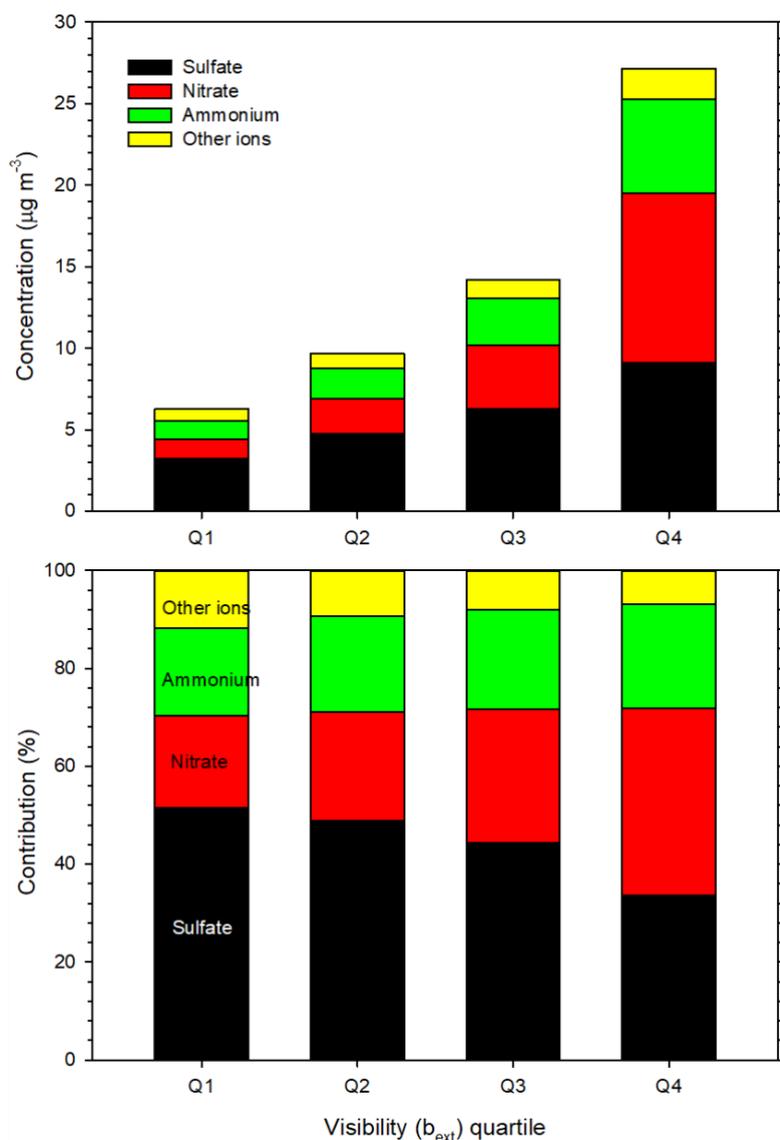
465

466 Fig. 3 The concentrations and contributions WSIs under different visibility classes,

467 Q1 (1st quartile; best visibility), Q2, Q3 and Q4 (poorest visibility).

468
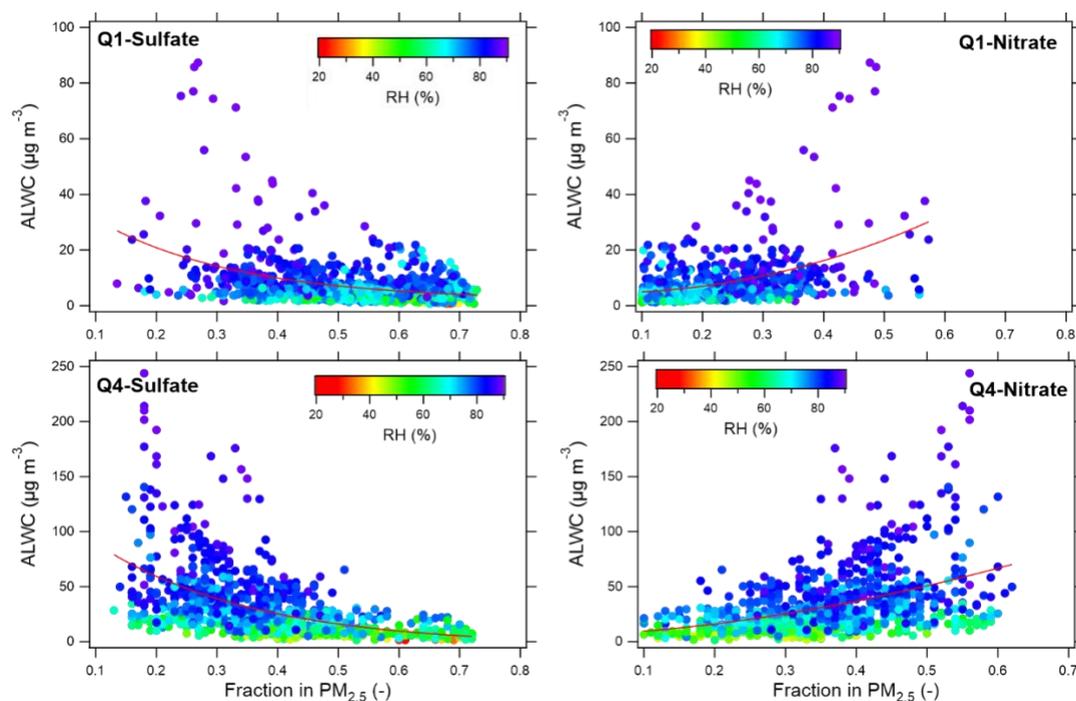
Fig. 4. The NO_3^- and SO_4^{2-} fractions in $PM_{2.5}$ as a function of ALWC and RH under best (Q1) and poorest (Q4) visibility.

Again, comparing Q1 and Q4, Fig. 5 shows the diurnal variations of hourly ALWC, aerosol pH, SOR and NOR. The hourly trends of all four variables were similar between Q1 and Q4, except that their average values were all higher in Q4 than in Q1. In addition, the variation of ALWC was considerably stronger in Q4 than in Q1. As expected, the ALWC and aerosol pH had minimum values near midday hours when the RH was the lowest, consistent with the fact that $[H^+]$ concentrations increases with lower ALWC. The SOR gradually increased during daytime and reached a maximum around 17:00 LT, and then decreased during nighttime. Unlike SOR, the maximum of NOR occurred earlier at 14:00 LT, coinciding with the O_3 peak, and then sharply dropped to a minimum at 18:00 LT. The decreasing trend of both NOR and NO_3^- (Fig. 1) was accompanied with increasing SOR. These results indicate that the formation of daytime NO_3^- and SO_4^{2-} were driven primarily by photochemical gas-phase reactions, during which the oxidation of sulfur was particularly more efficient and competitive than the oxidation of nitrogen in the afternoon. The average SOR and NOR were 0.31 and 0.10, respectively, during the study. On the other hand, since the NO_3^- and NOx increased during humid nighttime hours, the relatively low NOR suggests that the uptake and subsequent hydrolysis of N_2O_5 was likely responsible for the elevated NO_3^- during nighttime.
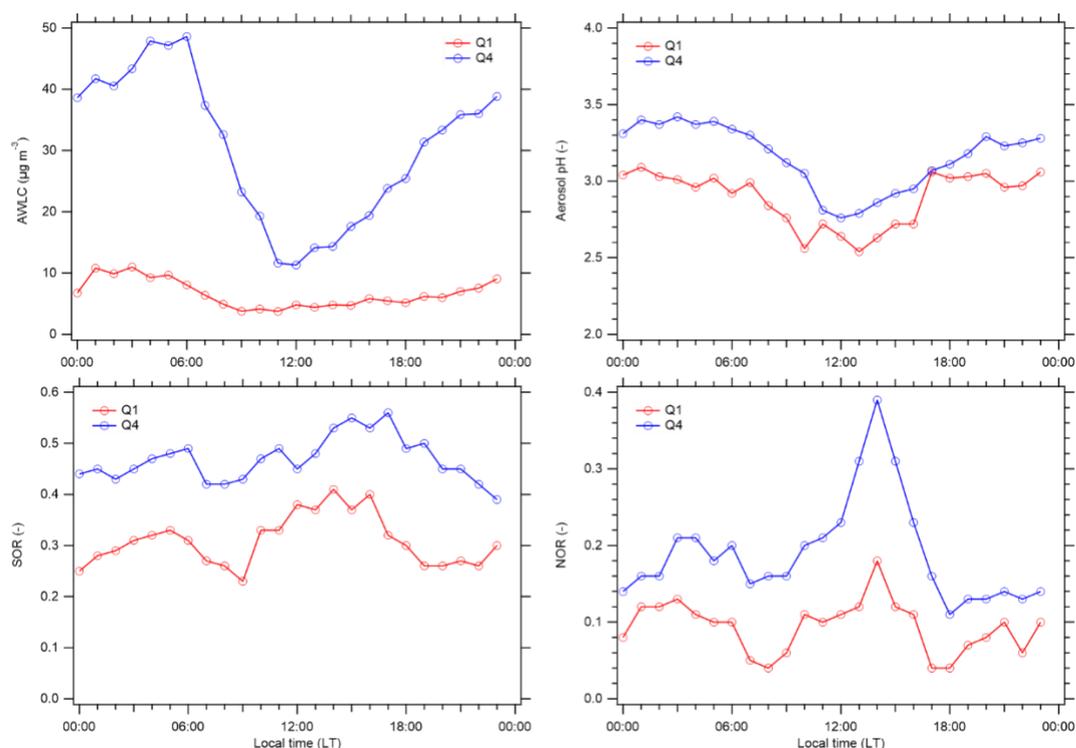
Fig. 5. The diurnal variations of hourly ALWC, aerosol pH, SOR and NOR under best (Q1) and poorest (Q4) visibility.

3.4 Ammonium neutralization and excess ammonia

Fig. 6 shows the relationships between the measured NH_4^+ versus the required NH_4^+ for complete neutralization of NO_3^- and SO_4^{2-}, and the measured TNH_3 versus the required TNH_3. The linear regression indicates that, on average, the excess NH_4^+ was about 24%, and the excess increased with increasing $PM_{2.5}$. Under high $PM_{2.5}$ (> 35 $\mu g\ m^{-3}$; the 24-hr average air quality standard), the NH_4^+ were more than enough to balance all the inorganic anions. Because the concentrations of nonvolatile cations (Na^+, K^+, Ca^{2+} and Mg^{2+}; Table 2) were quite low in the study area, the excess NH_4^+ are likely associated with organic acids (Kerminen et al., 2001). In addition, the measured TNH_3 substantially exceeded the required TNH_3 for the overall charge balance, and the excess amount increased with increasing NH_3. The measured NH_3 averaged 11.9 ± 5.8 ppb in this study (Table 1). It is clear that the inorganic aerosol system was under NH_4^+ and NH_3-excess condition in the study area. Similar ammonia-rich environments have been reported in large urban and livestock farming areas (Acharja et al., 2022; Cheng and Wang-Li, 2019; Duan et al., 2021).

18

516

517
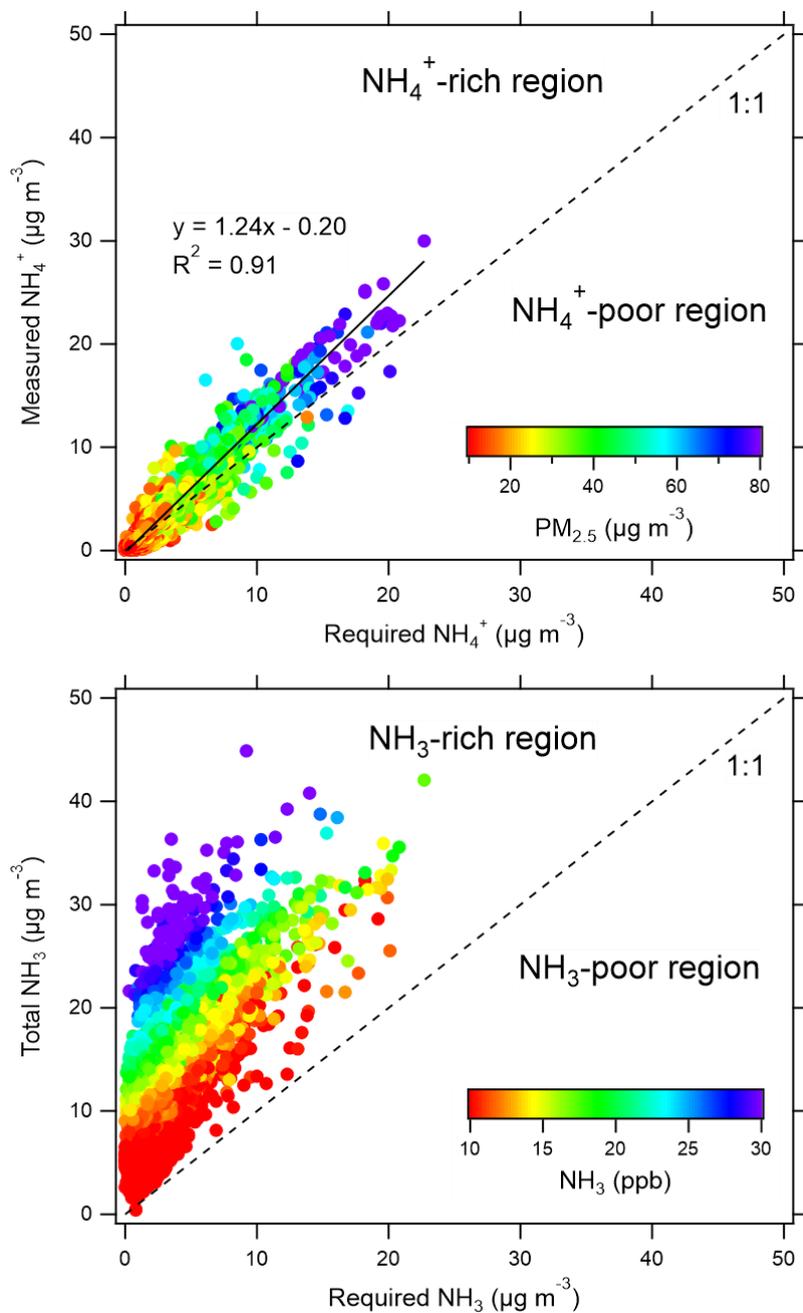
Fig. 6. The relationships between the measured NH_4^+ versus the required NH_4^+, and the measured TNH_3 versus the required TNH_3 under varying $PM_{2.5}$ and NH_3, respectively.

## 3.5 Gas-particle partitioning and PM sensitivity

The above results show that the severely impaired visibility was attributable to the elevated NO_3^- and ALWC under NH_3-excess condition. The question about how to control the NO_3^- formation arises as an important topic for air pollution abatement

527 and hence visibility improvement policy. Fig. 7(a) shows the dependency of $\varepsilon(NO_3^-)$

528 and $\varepsilon(NH_4^+)$ on the aerosol pH under 298 K and the observed average ALWC of 15.6

529 $\mu g\ m^{-3}$ in this study. The predicted average pH of 3.01 ± 0.52 is also plotted alongside

530 the x axis, at which the predicted $\varepsilon(NO_3^-)$ and $\varepsilon(NH_4^+)$ are 78.1% and 7.1%,

531 respectively. It is noted that the aerosol pH of this study is generally lower than that in

532 several China cities (Ding et al., 2019; Duan et al., 2021; Song et al., 2018), whereas

533 it is higher than that in several US cities (Guo et al., 2017, 2015; Nah et al., 2018).

534 Assuming a threshold of $\varepsilon(NO_3^-) = \varepsilon(NH_4^+) = 0.1$, the characteristic pH above which

535 $\varepsilon(NO_3^-)$ becomes sensitive to HNO_3 is 1.51 (shown as the purple plus white zone),

536 whereas that above which $\varepsilon(NH_4^+)$ becomes insensitive to NH_3 is 2.84 (white zone).

537 Given the observed ALWC ($15.6 \pm 19.3\ \mu g\ m^{-3}$) and aerosol pH ($3.01 \pm 0.52$), the

538 $PM_{2.5}$ in the study area is expected to respond strongly to the TNO_3^- ($= NO_3^- +$

539 HNO_3), i.e., the $PM_{2.5}$ is sensitive to HNO_3 and hence NOx. On the other hand, the

540 TNH_4^+ ($= NH_4^+ + NH_3$) predominantly resides in the gas phase as NH_3, and thus is

541 insensitive to NH_3. For the $PM_{2.5}$ to become sensitive ($\varepsilon(NO_3^-) = 0.5$) to NH_3, a 72%

542 reduction of NH_3 is required such that the aerosol pH would drop from its current

543 state of 3.01 to 2.46 (pH″ in Fig. 7(a)). The pH drop would in turn drive 50% of

544 aerosol NO_3^- to gas phase HNO_3. For a more substantial reduction of the $PM_{2.5}$ level

545 ($\varepsilon(NO_3^-) = 0.1$), a reduction of 95% reduction of NH_3 is required for the aerosol pH to

546 drop from 3.01 to 1.51 (pH′ in Fig. 7(a)). Such large NH_3 reductions are very difficult

547 to realize in the short run because the major sources of NH_3 in Taiwan are livestock

548 farming (41.5% contribution) and waste water treatment plants (29.1%), both of

549 which are considered fugitive emissions (Taiwan EPA, 2021) (Fig. S6). Unlike other

550 cities in Taiwan, the study area in Taichung has a unique, major fuel-combustion

551 source (27%), i.e., the largest coal-fired power plant in Taiwan. Even so, large NH_3

552 reductions are challenging and require long-term, comprehensive planning. Fig. 7(b)

553 more clearly shows the chemical domains of PM sensitivity under different visibility

554 classes (Q1 to Q4), with respect to aerosol pH and ALWC. The results indicate that

555 the aerosol pH becomes less variable whereas the ALWC increases with decreasing

556 visibility. In addition, as pointed out by Nenes et al. (Nenes et al., 2020), the transition

557 between HNO_3-sensitive and NH_3-sensitive domain occurs at aerosol pH≈2 over a

558 wide range of ALWC (1 to 100 $\mu g\ m^{-3}$). In this study, regardless of the visibility

559 classes, most of the data points fall in the HNO_3-sensitive domain. This is especially

560 the case under severely impaired visibility (Q4). As such, the reduction of HNO_3

561 would promptly result in the decrease of NO_3^-, $PM_{2.5}$ and hence improved visibility

562 because the above assessments are based on hourly data. Overall, the study area is

563 characterized by excessively high NH_3, as well as low nonvolatile cations, and thus

564 HNO_3 is the main limiting factor in the formation of inorganic $PM_{2.5}$.

565

566

567

568
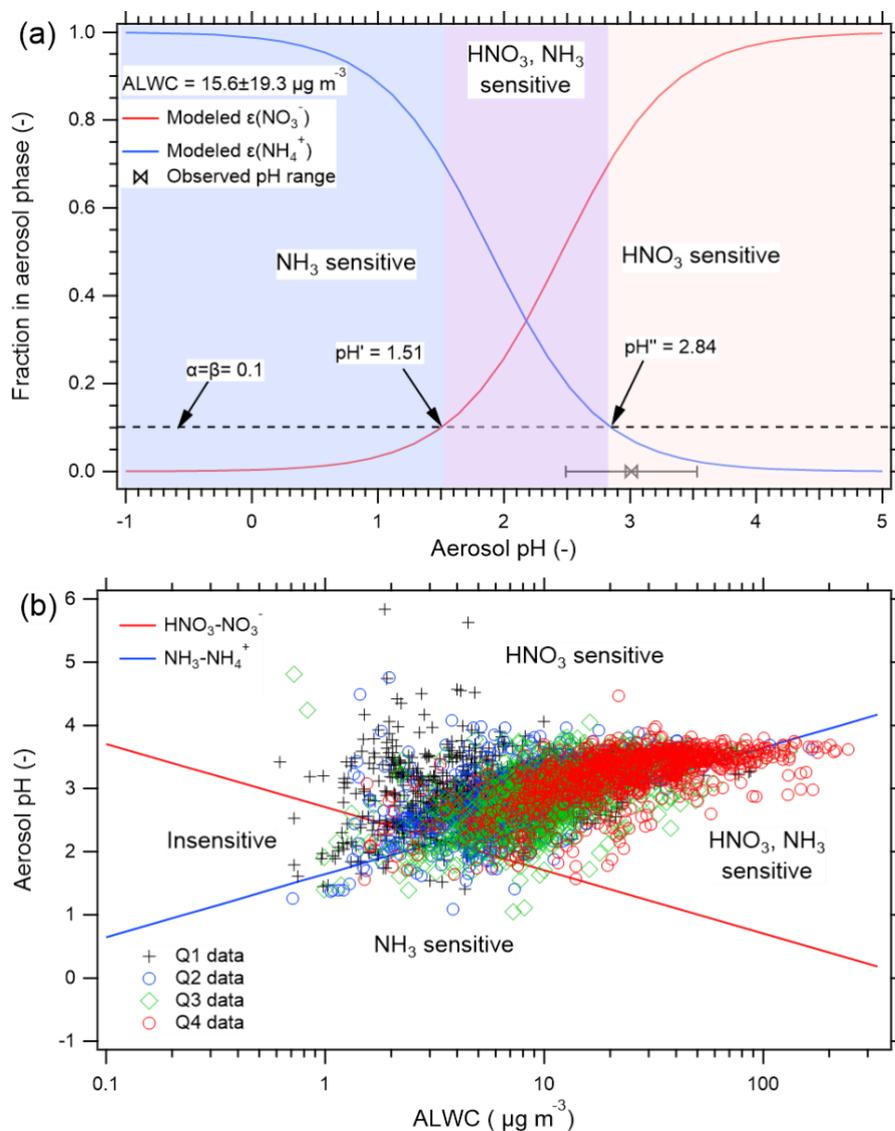
Fig. 7. The dependency of $\varepsilon(NO_3^-)$ and $\varepsilon(NH_4^+)$ on the aerosol pH, and the chemical
domains of PM sensitivity for different visibility classes, Q1 (best visibility), Q2, Q3
and Q4 (poorest visibility).

4. Conclusions

This study investigated the relationships between inorganic aerosol chemistry and
atmospheric visibility at an ammonia-rich urban area in Taiwan, based on long-term
hourly measurements of gas-phase NH_3, HNO_3, HCl and $PM_{2.5}$ water-soluble ions
WSIs SO_4^{2-}, NO_3^-, Cl^-, NH_4^+, Na^+, K^+, Ca^{2+} and Mg^{2+} from 2017 to 2019. The
thermodynamic equilibrium state of the inorganic aerosol system and the gas-particle
partitioning of volatile NH_4NO_3 were assessed using the ISORROPIA II model. On

580   average, the WSIs made up about 50% of the $PM_{2.5}$, with the major ions SO_4^{2-}, NO_3^-

581   and NH_4^+ (SNA) contributing to 90% of WSIs. The SNA had the lowest

582   concentrations in the summer, and higher concentration in the other seasons. The

583   diurnal variations of SNA, aerosol pH, aerosol liquid water content (ALWC) and

584   sulfur/nitrogen oxidation ratio (SOR/NOR) indicate that there were two different

585   processes driving the daytime and nighttime formation of elevated NO_3^-. In the

586   daytime, the gas-phase NO_2 oxidation and HNO_3 condensation were more important,

587   but being suppressed by the competition from SO_2 oxidation in the afternoon of

588   diminishing oxidants (e.g., OH and O_3). In the nighttime, the aqueous-phase uptake

589   and hydrolysis of N_2O_5 and the reduction of NO_3 radical were more prominent. The

590   elevated SO_4^{2-} formation was more associated with the gas-phase SO_2 oxidation in

591   the daytime. In addition, the diurnal variation of SO_4^{2-} clearly deviated from that of

592   NO_3^- and NH_4^+, particularly in the afternoon, indicating NO_3^- was the limiting factor

593   of elevated NH_4^+. The elevated NO_3^- were prevalence under stagnant condition and

594   thus of local origin, whereas the elevated SO_4^{2-} were related to regional transport

595   from the northwest-west area where the source strength is strong.

596   The $PM_{2.5}$, SNA and ALWC increased with decreasing atmospheric visibility, with

597   the maximum increase by a factor of about 4. The ambient "wet" $PM_{2.5}$ was a factor

598   of 1.79 higher than the measured "dry" $PM_{2.5}$. Among the SNA, the NO_3^- contribution

599   to the $PM_{2.5}$ increased substantially whereas the SO_4^{2-} contribution decreased with

600   decreasing visibility. The coupling of NO_3^- and ALWC were obvious under

601   decreasing visibility, indicating the mutual promotion between the two enhanced the

602   hygroscopicity and aqueous-phase reactions conducive for NO_3^- formation.

603   Interestingly, the RH appeared to be a required but not sufficient condition for

604   elevated NO_3^- formation; ALWC was more important. These results suggest that "dry"

605      $PM_{2.5}$ may not fully explain the impaired visibility, and the SNA and ALWC must also

606   be considered in the visibility assessment. Overall, the inorganic aerosol system in the

607   study area was characterized by excessive NH_3 and NH_4^+ under high RH (average

608   70.7%), where the $PM_{2.5}$ was sensitive to HNO_3 and hence NOx, and insensitive to

609   NH_3. Under such condition, the SO_4^{2-} was fully neutralized as $(NH_4)_2SO_4$ and thus

610   was not a limiting factor of impaired visibility. A reduction of SO_2 would cause a

611   decrease of SO_4^{2-}, but that reduction would be balanced by enhanced NO_3^- formation,

612   though the exact extent needs to be further examined. In contrast, a reduction of NOx

613   would result in an instantaneous reduction of NO_3^-, $PM_{2.5}$, ALWC, and hence

614   improved visibility. Lastly, a substantial amount of NH_3 reduction (73%) is required,

615   which is likely impractical in the short run, such that $PM_{2.5}$ becomes sensitive to NH_3.

616

623

Conflicts of Interest

624

625 The authors declare no conflicts of interest.

626

627 **References**

628 Acharja, P., Ali, K., Ghude, S.D., Sinha, V., Sinha, B., Kulkarni, R., Gultepe, I.,
629   Rajeevan, M.N., 2022. Enhanced secondary aerosol formation driven by excess
630   ammonia during fog episodes in Delhi, India. Chemosphere 289, 133155.
631   https://doi.org/10.1016/j.chemosphere.2021.133155

632 Cai, H., Gui, K., Chen, Q., 2018. Changes in Haze Trends in the Sichuan-Chongqing
633   Region, China, 1980 to 2016. Atmosphere 9, 277–17.
634   https://doi.org/10.3390/atmos9070277

635 Cao, J., Wang, Q., Chow, J.C., Watson, J.G., Tie, X., Shen, Z., Wang, P., An, Z.,
636   2012. Impacts of aerosol compositions on visibility impairment in Xi'an, China.
637   Atmos Environ 59, 559–566. https://doi.org/10.1016/j.atmosenv.2012.05.036

638 Cheng, B., Wang-Li, L., 2019. Responses of Secondary Inorganic PM2.5 to Precursor
639   Gases in an Ammonia Abundant Area In North Carolina. Aerosol and Air Quality
640   Research 19, 1126–1138. https://doi.org/10.4209/aaqr.2018.10.0384

641 Cheng, Z., Luo, L., Wang, S., Wang, Y., Sharma, S., Shimadera, H., Wang, X.,
642   Bressi, M., Miranda, R.M. de, Jiang, J., Zhou, W., Fajardo, O., Yan, N., Hao, J.,
643   2016. Status and characteristics of ambient PM2.5 pollution in global megacities.
644   Environ Int 89, 212–221. https://doi.org/10.1016/j.envint.2016.02.003

645 Cheng, Z., Ma, X., He, Y., Jiang, J., Wang, X., Wang, Y., Sheng, L., Hu, J., Yan, N.,
646   2017. Mass extinction efficiency and extinction hygroscopicity of ambient PM2.5
647   in urban China. Environmental Research 156, 239–246.
648   https://doi.org/10.1016/j.envres.2017.03.022

649 Chen, W.-N., Chen, Y.-C., Kuo, C.-Y., Chou, C.-H., Cheng, C.-H., Huang, C.-C.,
650   Chang, S.-Y., Raman, M.R., Shang, W.-L., Chuang, T.-Y., Liu, S.-C., 2014. The
651   real-time method of assessing the contribution of individual sources on visibility
652   degradation in Taichung. Science of The Total Environment 497–498, 219–228.
653   https://doi.org/10.1016/j.scitotenv.2014.07.120

654 Clegg, S.L., Brimblecombe, P., Wexler, A.S., 1998. Thermodynamic Model of the
655   System H+−NH4 +−Na+−SO4 2-−NO3 -−Cl-−H2O at 298.15 K. J Phys Chem
656   102, 2155–2171. https://doi.org/10.1021/jp973043j

657 Ding, J., Zhao, P., Su, J., Dong, Q., Du, X., Zhang, Y., 2019. Aerosol pH and its
658   driving factors in Beijing. Atmos Chem Phys 19, 7939–7954.
659   https://doi.org/10.5194/acp-19-7939-2019

660 Duan, X., Yan, Y., Peng, L., Xie, K., Hu, D., Li, R., Wang, C., 2021. Role of
661   ammonia in secondary inorganic aerosols formation at an ammonia-rich city in
662   winter in north China: A comparative study among industry, urban, and rural sites.
663   Environ Pollut 291, 118151. https://doi.org/10.1016/j.envpol.2021.118151

664 Feng, T., Bei, N., Zhao, S., Wu, J., Li, X., Zhang, T., Cao, J., Zhou, W., Li, G., 2018.
665   Wintertime nitrate formation during haze days in the Guanzhong basin, China: A
666   case study. Environmental Pollution 243, 1057–1067.
667   https://doi.org/10.1016/j.envpol.2018.09.069

668 Fierz-Schmidhauser, R., Zieger, P., Wehrle, G., Jefferson, A., Ogren, J.A.,
669   Baltensperger, U., Weingartner, E., 2010. Measurement of relative humidity
670   dependent light scattering of aerosols. Atmos Meas Tech 3, 39–50.
671   https://doi.org/10.5194/amt-3-39-2010

672 Fountoukis, C., Nenes, A., 2007. ISORROPIA II: a computationally efficient
673   thermodynamic equilibrium model for K+−Ca2+−Mg2+−NH4+−Na+−SO42−−
674   NO3−−Cl−−H2O aerosols. Atmospheric Chemistry and Physics 49, 793–801.
675   https://doi.org/10.1080/02786826.2015.1073848

676 Fountoukis, C., Nenes, A., Sullivan, A., 2009. Thermodynamic characterization of
677   Mexico City aerosol during MILAGRO 2006. Atmospheric Chemistry and Physics
678   9, 2141–2156. https://doi.org/10.5194/acp-9-2141-2009

679 Fu, X., Wang, T., Gao, J., Wang, P., Liu, Y., Wang, S., Zhao, B., Xue, L., 2020.
680   Persistent Heavy Winter Nitrate Pollution Driven by Increased Photochemical
681   Oxidants in Northern China. Environ Sci Technol 54, 3881–3889.
682   https://doi.org/10.1021/acs.est.9b07248

683 Fu, X., Wang, X., Hu, Q., Li, G., Ding, X., Zhang, Y., He, Q., Liu, T., Zhang, Z., Yu,
684   Q., Shen, R., Bi, X., 2016. Changes in visibility with PM2.5 composition and
685   relative humidity at a background site in the Pearl River Delta region. Journal of
686   environmental sciences (China) 40, 10–19.
687   https://doi.org/10.1016/j.jes.2015.12.001

688 Griffith, S.M., Huang, X.H.H., Louie, P.K.K., Yu, J.Z., 2015. Characterizing the
689   thermodynamic and chemical composition factors controlling PM2.5 nitrate:
690   Insights gained from two years of online measurements in Hong Kong.

Atmospheric Environment 122, 864–875.
https://doi.org/10.1016/j.atmosenv.2015.02.009

Guo, H., Liu, J., Froyd, K.D., Roberts, J.M., Veres, P.R., Hayes, P.L., Jimenez, J.L., Nenes, A., Weber, R.J., 2017. Fine particle pH and gas–particle phase partitioning of inorganic species in Pasadena, California, during the 2010 CalNex campaign. Atmospheric Chemistry and Physics 17, 5703–5719. https://doi.org/10.5194/acp-17-5703-2017

Guo, H., Otjes, R., Schlag, P., Kiendler-Scharr, A., Nenes, A., Weber, R.J., 2018. Effectiveness of ammonia reduction on control of fine particle nitrate. Atmospheric Chemistry and Physics 18, 12241–12256. https://doi.org/10.5194/acp-18-12241-2018

Guo, H., Xu, L., Bougiatioti, A., Cerully, K.M., Capps, S.L., Jr, J.R.H., Carlton, A.G., Lee, S.H., Bergin, M.H., Ng, N.L., Nenes, A., Weber, R.J., 2015. Fine-particle water and pH in the southeastern United States. Atmospheric Chemistry and Physics 15, 5211–5228. https://doi.org/10.5194/acp-15-5211-2015

Hu, S., Zhao, G., Tan, T., Li, C., Zong, T., Xu, N., Zhu, W., Hu, M., 2021. Current challenges of improving visibility due to increasing nitrate fraction in PM2.5 during the haze days in Beijing, China. Environ Pollut 290, 118032. https://doi.org/10.1016/j.envpol.2021.118032

Kerminen, V.M., Hillamo, R., Teinilä, K., Pakkanen, T., 2001. Ion balances of size-resolved tropospheric aerosol samples: implications for the acidity and atmospheric processing of aerosols 35, 5255–5265. https://doi.org/10.1016/s1352-2310(01)00345-4

Lee, C.-G., Yuan, C.-S., Chang, J., Yuan, C., 2012. Effects of Aerosol Species on Atmospheric Visibility in Kaohsiung City, Taiwan. Journal of the Air & Waste Management Association 55, 1031–1041. https://doi.org/10.1080/10473289.2005.10464683

Liang, C.-S., Duan, F.-K., He, K.-B., Ma, Y.-L., 2016. Review on recent progress in observations, source identifications and countermeasures of PM2.5. Environ Int 86, 150–170. https://doi.org/10.1016/j.envint.2015.10.016

Liu, M., Song, Y., Zhou, T., Xu, Z., Yan, C., Zheng, M., Wu, Z., Hu, M., Wu, Y., Zhu, T., 2017. Fine particle pH during severe haze episodes in northern China. Geophys Res Lett 44, 5213–5221. https://doi.org/10.1002/2017gl073210

Liu, Y., Zheng, M., Yu, M., Cai, X., Du, H., Li, J., Zhou, T., Yan, C., Wang, X., Shi, Z., Harrison, R.M., Zhang, Q., He, K., 2019. High-time-resolution source apportionment of PM2.5 in Beijing with multiple models. Atmospheric Chemistry and Physics 19, 6595–6609. https://doi.org/10.5194/acp-19-6595-2019

728   Luan, T., Guo, X., Guo, L., Zhang, T., 2018. Quantifying the relationship between
729   PM2.5 concentration, visibility and planetary boundary layer height for long-
730   lasting haze and fog–haze mixed events in Beijing. Atmospheric Chemistry and
731   Physics 18, 203–225. https://doi.org/10.5194/acp-18-203-2018

732   Malm, W.C., Sisler, J.F., Huffman, D., Eldred, R.A., Cahill, T.A., 1994. Spatial and
733   seasonal trends in particle concentration and optical extinction in the United States.
734   Journal of Geophysical Research 99, 1347–1370.

735   Maurer, M., Klemm, O., Lokys, H.L., Lin, N.-H., 2019. Trends of Fog and Visibility
736   in Taiwan: Climate Change or Air Quality Improvement? Aerosol Air Qual Res
737   19, 896–910. https://doi.org/10.4209/aaqr.2018.04.0152

738   Meng, Z., Seinfeld, J.H., 1996. Time scales to achieve atmospheric gas-aerosol
739   equilibrium for volatile species. Atmos Environ 30, 2889–2900.
740   https://doi.org/10.1016/1352-2310(95)00493-9

741   Myhre, G., Shindell, D., Bréon, F.-M., Collins, W., Fuglestvedt, J., 2013.
742   Anthropogenic and Natural Radiative Forcing.

743   Nah, T., Guo, H., Sullivan, A.P., Chen, Y., Tanner, D.J., Nenes, A., Russell, A., Ng,
744   N.L., Huey, L.G., Weber, R.J., 2018. Characterization of aerosol composition,
745   aerosol acidity, and organic acid partitioning at an agriculturally intensive rural
746   southeastern US site. Atmos Chem Phys 18, 11471–11491.
747   https://doi.org/10.5194/acp-18-11471-2018

748   Nenes, A., Pandis, S.N., Pilinis, C., 1999. Continued development and testing of a
749   new thermodynamic aerosol module for urban and regional air quality models.
750   Atmospheric Environment 33, 1553–1560. https://doi.org/10.1016/s1352-
751   2310(98)00352-5

752   Nenes, A., Pandis, S.N., Weber, R.J., Russell, A., 2020. Aerosol pH and liquid water
753   content determine when particulate matter is sensitive to ammonia and nitrate
754   availability. Atmos Chem Phys 20, 3249–3258. https://doi.org/10.5194/acp-20-
755   3249-2020

756   Pitchford, M., Maim, W., Schichtel, B., Kumar, N., Lowenthal, D., Hand, J., 2007.
757   Revised algorithm for estimating light extinction from IMPROVE particle
758   speciation data. Journal of the Air & Waste Management Association (1995) 57,
759   1326–1336. https://doi.org/10.3155/uawm20.v057.i11;article:article:10.3155/1047-
760   3289.57.11.1326;journal:journal:uawm20;wgroup:string:publication

761   Pope, C.A., Coleman, N., Pond, Z.A., Burnett, R.T., 2020. Fine particulate air
762   pollution and human mortality_ 25+ years of cohort studies. Environmental
763   Research 183, 108924. https://doi.org/10.1016/j.envres.2019.108924

764 Pui, D.Y.H., Chen, S.-C., Zuo, Z., 2014. PM2.5 in China: Measurements, sources,
765   visibility and health effects, and mitigation. Particuology 13, 1–26.
766   https://doi.org/10.1016/j.partic.2013.11.001

767 Pye, H.O.T., Nenes, A., Alexander, B., Ault, A.P., Barth, M.C., Clegg, S.L., Jr.,
768   J.L.C., Fahey, K.M., Hennigan, C.J., Herrmann, H., Kanakidou, M., Kelly, J.T.,
769   Ku, I.-T., McNeill, V.F., Riemer, N., Schaefer, T., Shi, G., Tilgner, A., Walker,
770   J.T., Wang, T., Weber, R., Xing, J., Zaveri, R.A., Zuend, A., 2020. The acidity of
771   atmospheric particles and clouds. Atmospheric Chemistry and Physics 20, 4809–
772   4888. https://doi.org/10.5194/acp-20-4809-2020

773 See, S.W., Balasubramanian, R., Wang, W., 2006. A study of the physical, chemical,
774   and optical properties of ambient aerosol particles in Southeast Asia during hazy
775   and nonhazy days. J Geophys Res Atmospheres 1984 2012 111, n/a-n/a.
776   https://doi.org/10.1029/2005jd006180

777 Seinfeld, J.H., Pandis, S.N., 2016. Atmospheric Chemistry and Physics: From Air
778   Pollution to Climate Change, 3rd Ed. Wiley.

779 Shen, G., Xue, M., Yuan, S., Zhang, J., Zhao, Q., Li, B., Wu, H., Ding, A., 2014.
780   Chemical compositions and reconstructed light extinction coefficients of
781   particulate matter in a mega-city in the western Yangtze River Delta, China.
782   Atmospheric Environment 83, 14–20.
783   https://doi.org/10.1016/j.atmosenv.2013.10.055

784 Song, S., Gao, M., Xu, W., Shao, J., Shi, G., Wang, S., Wang, Y., Sun, Y., McElroy,
785   M.B., 2018. Fine-particle pH for Beijing winter haze as inferred from different
786   thermodynamic equilibrium models. Atmospheric Chemistry and Physics 18,
787   7423–7438. https://doi.org/10.5194/acp-18-7423-2018

788 Szidat, S., 2009. Sources of Asian Haze. Science 323, 470–471.
789   https://doi.org/10.1126/science.1169407

790 Taiwan Environmental Protection Administration (EPA). Taiwan Emission Data
791   System (TEDS). 2021 https://teds.epa.gov.tw/ (accessed June 16, 2021).

792 Tian, M., Liu, Y., Yang, F., Zhang, L., Peng, C., Chen, Y., Shi, G., Wang, H., Luo,
793   B., Jiang, C., Li, B., Takeda, N., Koizumi, K., 2019. Increasing importance of
794   nitrate formation for heavy aerosol pollution in two megacities in Sichuan Basin,
795   southwest China. Environmental Pollution 250, 898–905.
796   https://doi.org/10.1016/j.envpol.2019.04.098

797 Ting, Y.-C., Young, L.-H., Lin, T.-H., Tsay, S.-C., Chang, K.-E., Hsiao, T.-C., 2021.
798   Quantifying the impacts of PM2.5 constituents and relative humidity on visibility
799   impairment in a suburban area of eastern Asia using long-term in-situ
800   measurements. Sci Total Environ 151759.
801   https://doi.org/10.1016/j.scitotenv.2021.151759

802   Tsai, Y.I., 2005. Atmospheric visibility trends in an urban area in Taiwan 1961–2003.
803   Atmospheric Environment 39, 5555–5567.
804   https://doi.org/10.1016/j.atmosenv.2005.06.012
805   Tsai, Y.I., Cheng, M.T., 1999. Visibility and aerosol chemical compositions near the
806   coastal area in Central Taiwan. Science of The Total Environment 231, 37–51.
807   Tsai, Y.I., Kuo, S.-C., Lee, W.-J., Chen, C.-L., Chen, P.-T., 2007. Long-term
808   visibility trends in one highly urbanized, one highly industrialized, and two Rural
809   areas of Taiwan. Science of The Total Environment 382, 324–341.
810   https://doi.org/10.1016/j.scitotenv.2007.04.048
811   Wang, X., Wang, W., Yang, L., Gao, X., Nie, W., Yu, Y., Xu, P., Zhou, Y., Wang, Z.,
812   2012. The secondary formation of inorganic aerosols in the droplet mode through
813   heterogeneous aqueous reactions under haze conditions. Atmos Environ 63, 68–76.
814   https://doi.org/10.1016/j.atmosenv.2012.09.029
815   Wang, Y., Chen, Y., Wu, Z., Shang, D., Bian, Y., Du, Z., Schmitt, S.H., Su, R.,
816   Gkatzelis, G.I., Schlag, P., Hohaus, T., Voliotis, A., Lu, K., Zeng, L., Zhao, C.,
817   Alfarra, M.R., McFiggans, G., Wiedensohler, A., Kiendler-Scharr, A., Zhang, Y.,
818   Hu, M., 2020. Mutual promotion between aerosol particle liquid water and
819   particulate nitrate enhancement leads to severe nitrate-dominated particulate matter
820   pollution and low visibility. Atmospheric Chemistry and Physics 20, 2161–2175.
821   https://doi.org/10.5194/acp-20-2161-2020
822   Watson, J.G., 2002. Visibility: Science and Regulation. J Air Waste Manage 52, 628–
823   713. https://doi.org/10.1080/10473289.2002.10470813
824   Wen, L., Chen, J., Yang, L., Wang, X., Xu, C., Sui, X., Yao, L., Zhu, Y., Zhang, J.,
825   Zhu, T., Wang, W., 2015. Enhanced formation of fine particulate nitrate at a rural
826   site on the North China Plain in summer: The important roles of ammonia and
827   ozone. Atmos Environ 101, 294–302.
828   https://doi.org/10.1016/j.atmosenv.2014.11.037
829   Wexler, A.S., Seinfeld, J.H., 1990. The distribution of ammonium salts among a size
830   and composition dispersed aerosol. Atmospheric Environ Part Gen Top 24, 1231–
831   1246. https://doi.org/10.1016/0960-1686(90)90088-5
832   Wu, C., Wang, G., Cao, C., Li, Jianjun, Li, Jin, Wu, F., Huang, R., Cao, J., Han, Y.,
833   Ge, S., Xie, Y., Xue, G., Wang, X., 2019. Chemical characteristics of airborne
834   particles in Xi'an, inland China during dust storm episodes: Implications for
835   heterogeneous formation of ammonium nitrate and enhancement of N-deposition.
836   Environ Pollut 244, 877–884. https://doi.org/10.1016/j.envpol.2018.10.019
837   Yi, H., Zhang, J., Xiao, H., Tong, L., Cai, Q., Lin, J., Yu, W., Johnson, M.S., 2020.
838   Compact Algorithms for Predicting of Atmospheric Visibility Using PM2.5,

839   Relative Humidity and NO2. Aerosol Air Qual Res.

840   https://doi.org/10.4209/aaqr.2019.06.0286

841   Young, L.-H., Li, C.-H., Lin, M.-Y., Hwang, B.-F., Hsu, H.-T., Chen, Y.-C., Jung, C.-

842   R., Chen, K.-C., Cheng, D.-H., Wang, V.-S., Chiang, H.-C., Tsai, P.-J., 2016. Field

843   performance of a semi-continuous monitor for ambient PM2.5 water-soluble

844   inorganic ions and gases at a suburban site. Atmospheric Environment 144, 376–

845   388. https://doi.org/10.1016/j.atmosenv.2016.08.062

846   Yuan, C.-S., Lee, C.-G., Liu, S.-H., Yuan, C., Yang, H.-Y., Chen, C.-T.A., 2002.

847   Developing Strategies for Improving Urban Visual Air Quality. Aerosol Air Qual

848   Res 2, 9–22. https://doi.org/10.4209/aaqr.2002.06.0002

849   Yu, C., Wang, Z., Xia, M., Fu, X., Wang, W., Tham, Y.J., Chen, T., Zheng, P., Li, H.,

850   Shan, Y., Wang, X., Xue, L., Zhou, Y., Yue, D., Ou, Y., Gao, J., Lu, K., Brown,

851   S.S., Zhang, Y., Wang, T., 2020. Heterogeneous N2O5 reactions on atmospheric

852   aerosols at four Chinese sites: improving model representation of uptake

853   parameters. Atmos Chem Phys 20, 4367–4378. https://doi.org/10.5194/acp-20-

854   4367-2020

855   Yu, S., Dennis, R., Roselle, S., Nenes, A., Walker, J., Eder, B., Schere, K., Swall, J.,

856   Robarge, W., 2005. An assessment of the ability of three-dimensional air quality

857   models with current thermodynamic equilibrium models to predict aerosol NO3−.

858   Journal of Geophysical Research: Atmospheres (1984–2012) 110, D07S13.

859   https://doi.org/10.1029/2004jd004718

860   Zhang, J., Chameides, W.L., Weber, R., Cass, G., Orsini, D., 2002. An evaluation of

861   the thermodynamic equilibrium assumption for fine particulate composition:

862   Nitrate and ammonium during the 1999 Atlanta Supersite Experiment. Journal of

863   Geophysical Research 108, 8414. https://doi.org/10.1029/2001jd001592

864   Zhang, Z., Guan, H., Xiao, Hongwei, Liang, Y., Zheng, N., Luo, L., Liu, C., Fang, X.,

865   Xiao, Huayun, 2021. Oxidation and sources of atmospheric NOx during winter in

866   Beijing based on δ18O-δ15N space of particulate nitrate. Environ Pollut 276,

867   116708. https://doi.org/10.1016/j.envpol.2021.116708

868   Zhou, M., Qiao, L., Zhu, S., Li, L., Lou, S., Wang, H., Wang, Q., Tao, S., Huang, C.,

869   Chen, C., 2016. Chemical characteristics of fine particles and their impact on

870   visibility impairment in Shanghai based on a 1-year period observation. Journal of

871   environmental sciences (China) 48, 151–160.

872   https://doi.org/10.1016/j.jes.2016.01.022

873

874

875

876 **Insights to the hourly inorganic aerosol chemistry and its impact on atmospheric**
877 **visibility in an ammonia-rich urban area in central Taiwan**
878
879 **Supplemental material**
880
881 Captions:
882 Table S1. The method detection limits (MDL) of the semi-continuous inorganic gases
883 and aerosol composition (IGAC) monitor for water-soluble ions.
884 Table S2. The relationships between the ISORROPIA-predicted and measured
885 inorganic gases and $PM_{2.5}$ water-soluble ions.
886 Table S3. The meteorological condition and air quality during the study period.
887
888 Fig. S1. A map of the study area and sampling sites (star: main site; circle: satellite
889 site) and surrounding major stationary sources (diamond: power plant; square: steel
890 plant; triangle: Taichung port; shaded area: industrial or science park).
891 Fig. S2. The relationships between the molar equivalent concentrations of cations,
892 anions, NH_4^+, SO_4^{2-}, and $SO_4^{2-}+NO_3^-$.
893 Fig. S3. The wind rose during the study period.
894 Fig. S4. The monthly averages of SO_4^{2-}, NO_3^- and NH_4^+ during the study period.
895 Fig. S5. The non-parametric wind regression (NWR) plots for NO_2, NH_3, SO_2, NO_3^-,
896 NH_4^+ and SO_4^{2-}.
897 Fig. S6. The ambient "wet" $PM_{2.5}$ (=$PM_{2.5}$ + ALWC) versus the BAM-measured "dry"
898 $PM_{2.5}$ under varying RH.
899 Fig. S7. Primary emission sources of NH_3 in Taiwan (Taiwan EPA, 2021).
900
901

902

Table S1. The method detection limits (MDL) of the semi-continuous inorganic gases and aerosol composition (IGAC) monitor for water-soluble ions.

Species	MDL in solution[a] ppb	MDL in air[b] $\mu g/m^3$
Na^+	2.3	0.06
NH_4^+	2.1	0.05
K^+	2.0	0.05
Mg^{2+}	4.7	0.12
Ca^{2+}	2.8	0.07
Cl^-	2.7	0.07
NO_2^-	2.5	0.05
NO_3^-	4.3	0.11
SO_4^{2-}	3.3	0.08

a. The average solution collected per hour by IGAC is 25 ml.

b. The average air volume collected per hour is 24 m^3.

903

904

905

Table S2. The relationships between the ISORROPIA-
predicted and measured inorganic gases and PM$_{2.5}$ water-
soluble ions.

Species	Linear regression		
	Slope	Intercept	R^2
NH$_3$	1.11	-0.29	0.95
HCl	0.33	0.12	0.24
HNO$_3$	2.60	0.03	0.44
Na$^+$	1.00	0.00	1.00
NH$_4^+$	0.71	0.09	0.91
K$^+$	1.00	0.00	1.00
Ca^{2+}	0.96	0.01	1.00
Cl$^-$	0.85	-0.19	0.84
NO$_3^-$	0.97	-0.66	0.94
SO$_4^{2-}$	1.00	0.00	1.00

Linear equation: predicted = slope × observed + intercept
The sample size (N) is 5508 (hourly data).

915
916
917
918

Table S3. The meteorological condition and air quality during the study period.

	Temp. (°C)	RH (%)	Wind speed (m s^{-1})	PM$_{10}$	PM$_{2.5}$	SO$_2$	CO	O$_3$	NO	NO$_2$
N	5500	5483	5492	5391	5344	5381	5425	5426	5324	5412
Mean	22.4	70.7	1.4	37.7	22.9	2.3	0.46	28.0	4.8	18.3
SD	5.3	13.0	0.8	25.0	15.4	1.2	0.24	18.5	9.3	10.0
RSD	0.24	0.18	0.52	0.66	0.67	0.50	0.53	0.66	1.92	0.55

N is the sample size (hourly data), SD is the standard deviation, and RSD is the relative standard deviation.

PM is in μg m^{-3}, CO in ppm and other gaseous species in ppb.

919
920
921
922
923
924
925
926
927
928
929
930
931
932
933
934
935
936
937
938
939
940
941

942

943
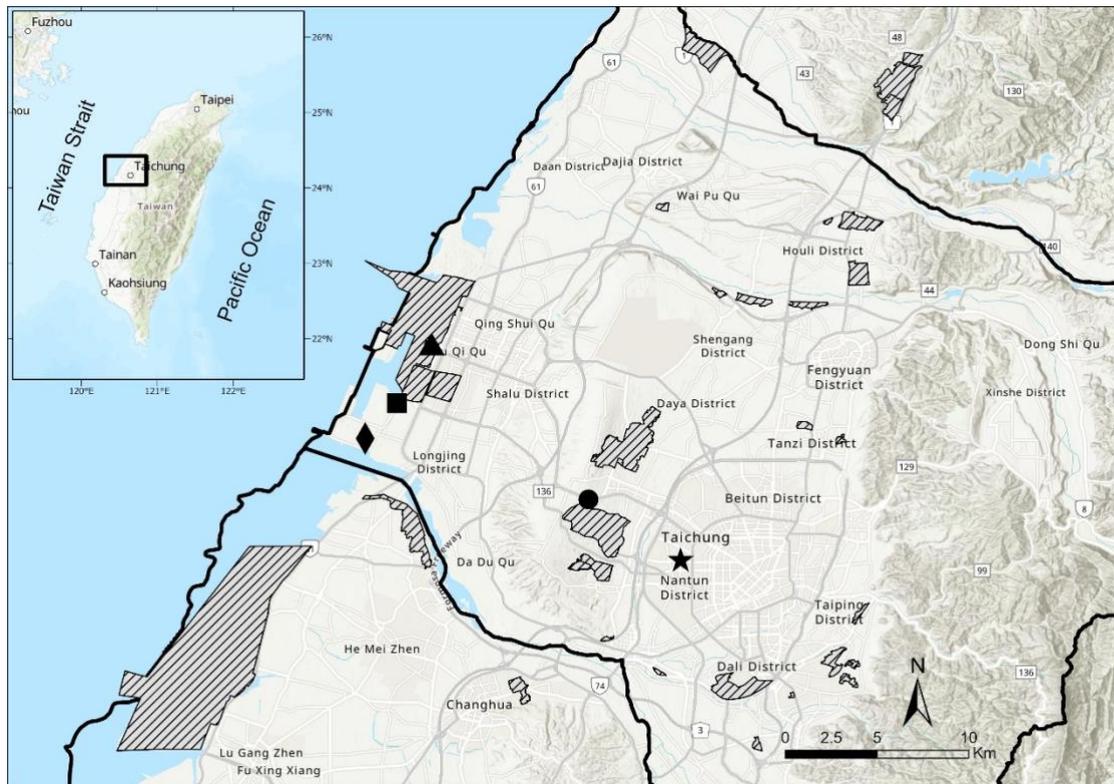
944

Fig. S1. A map of the study area and sampling sites (star: main site; circle: satellite site) and surrounding major stationary sources (diamond: power plant; square: steel plant; triangle: Taichung port; shaded area: industrial or science park).

948

949
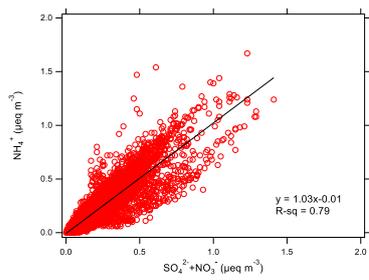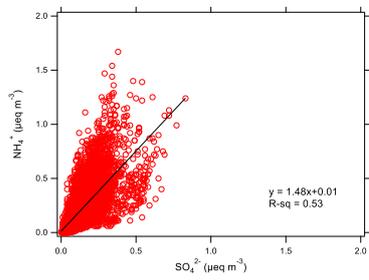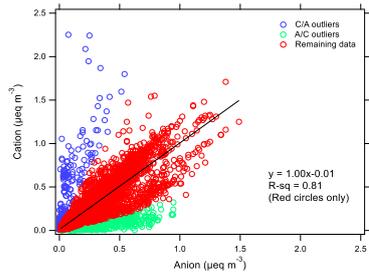
950

951   Fig. S2. The relationships between the molar equivalent concentrations of cations,

952   anions, NH_4^+, SO_4^{2-}, and $SO_4^{2-}+NO_3^-$.

953
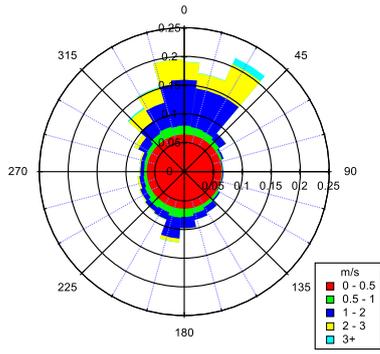
954

955   Fig. S3. The wind rose during the study period.

956

957
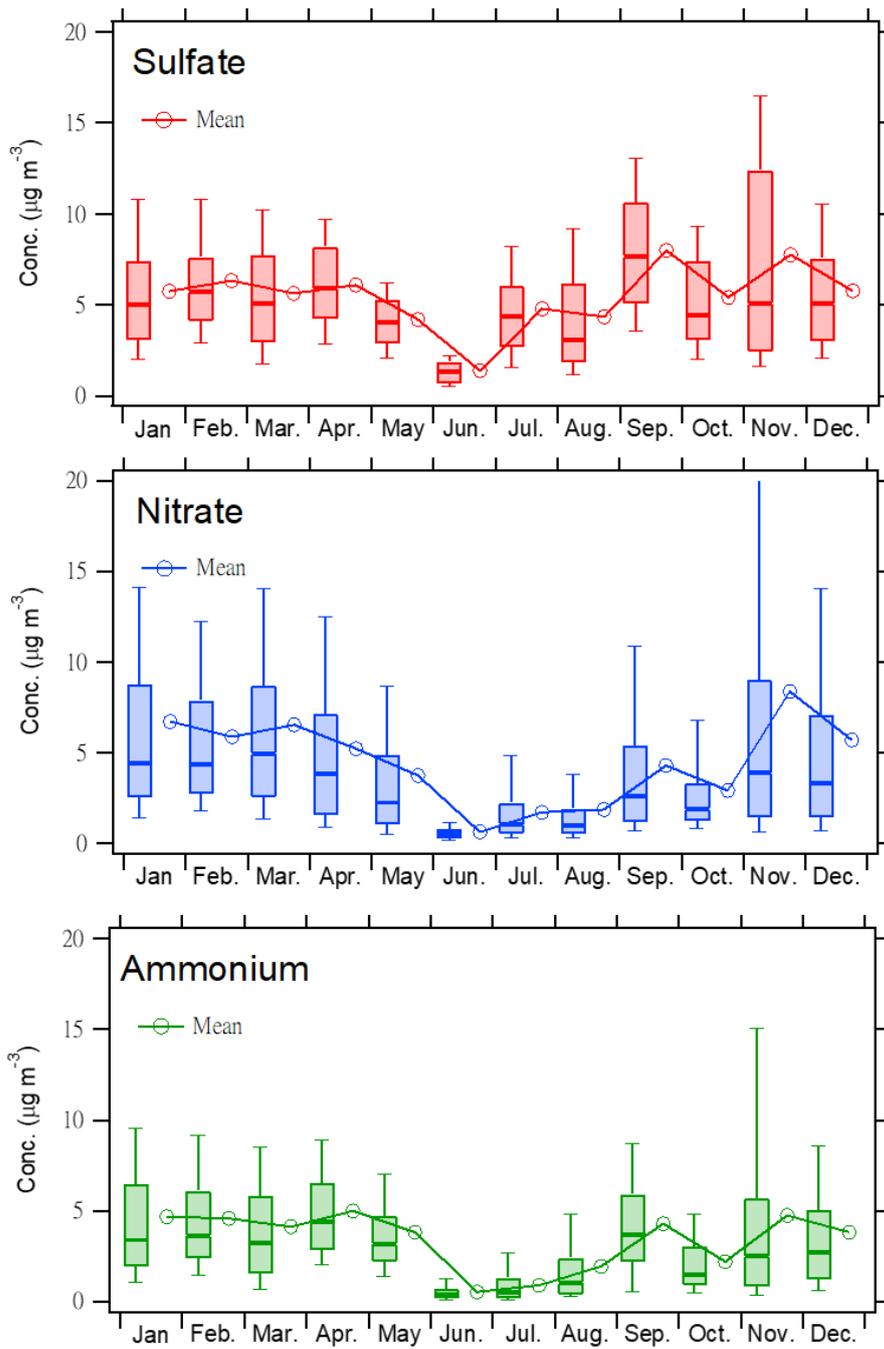
958

959   Fig. S4. The monthly averages of SO_4^{2-}, NO_3^- and NH_4^+ during the study period.

960

961

962
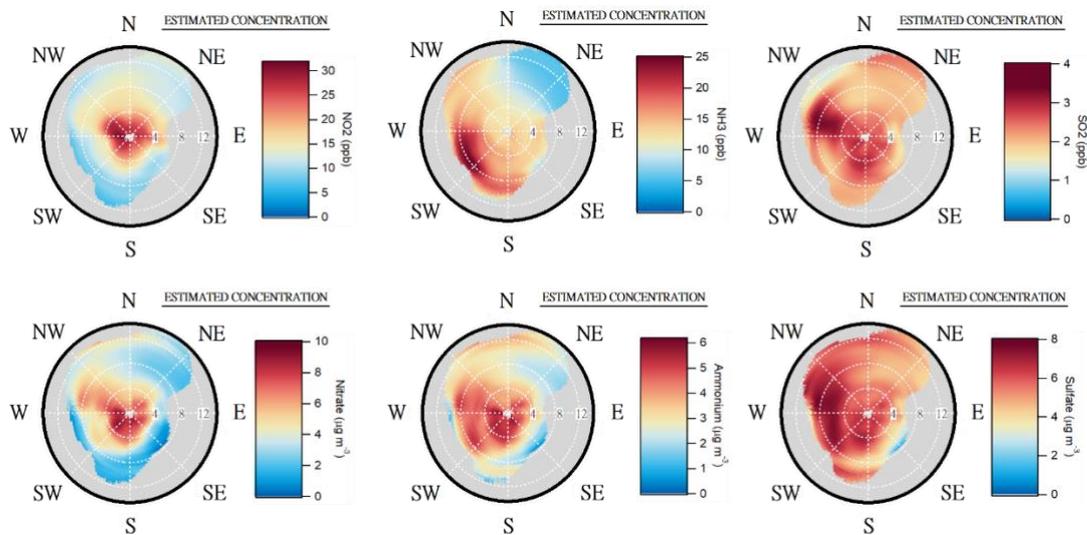
963

Fig. S5. The non-parametric wind regression (NWR) plots for NO_2, NH_3, SO_2, NO_3^-, NH_4^+ and SO_4^{2-}.

966

967

968
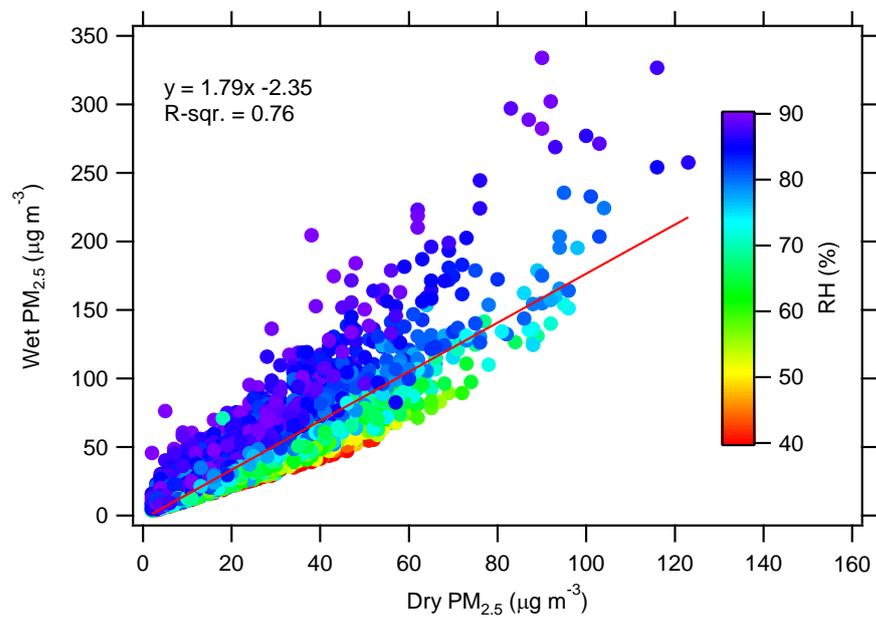
969

Fig. S6. The ambient "wet" $PM_{2.5}$ (=$PM_{2.5}$ + ALWC) versus the BAM-measured "dry" $PM_{2.5}$ under varying RH.

970

971

972

973

974

NH$_3$ emission (tons/yr)

- Waste water treatment plants
- Livestock farming
- Human bioeffluent
- Plants
- Agriculture fertilizer
- Fuel combustion

29.1%

41.5%

6.5%

7.5%

3.6%

11.9%
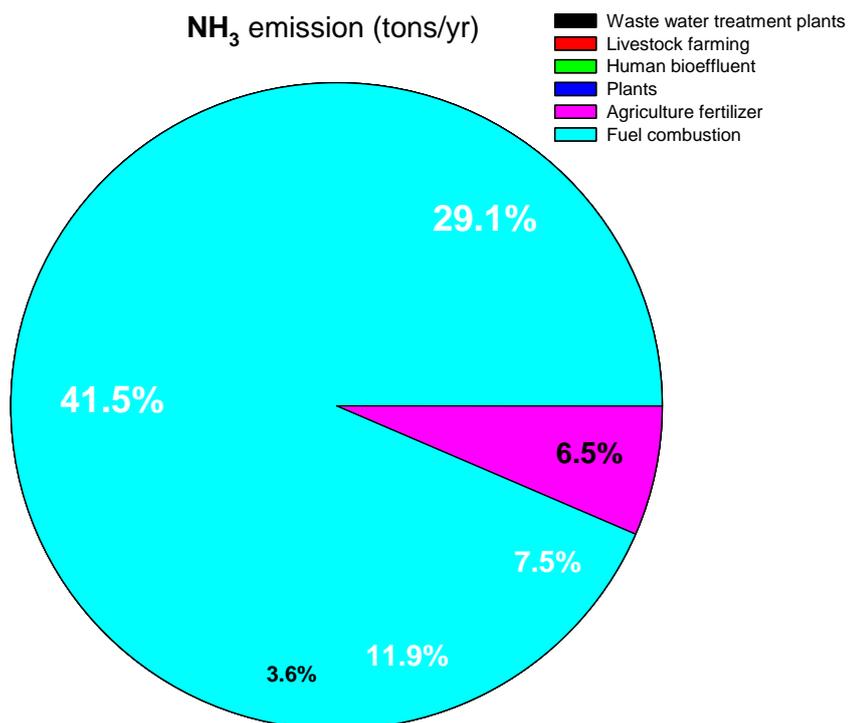
975

976   Fig. S7. Primary emission sources of NH$_3$ in Taiwan (Taiwan EPA, 2021).

977

978